Received: 19 September 2025 | Revised: 15 April 2026 | Accepted: 29 May 2026

DOI: 10.1002/qj.70244

Quarterly Journal of the Royal Meteorological Society RMetS

RESEARCH ARTICLE

Scale dependence of the marine atmospheric boundary-layer response to ocean surface-temperature variability in the EUREC^{4}A region

Alessandro Storer | **Matteo Borgnino** | **Claudia Pasquero** | **Agostino Niyonkuru Meroni**

Department of Environmental and Earth Sciences, University of Milan Bicocca, Milan, Italy

Correspondence
Alessandro Storer and Agostino Niyonkuru Meroni, Department of Environmental and Earth Sciences, University of Milan Bicocca, Piazza della Scienza 4, 20126 Milan, Italy.
Email: alessandro.storer@unimib.it and agostino.meroni@unimib.it

Funding information
Istituto Nazionale di Oceanografia e Geofisica Sperimentale (OGS), Grant/Award Number: HPC-TRES 2023-04; Joint Programming Initiative Climate and Oceans, Grant/Award Number: EUREC^{4}A-OA

Abstract

A large share of energy within the global oceans lies within the mesoscale range, $\mathcal{O}(100\,\text{km})$, where very large dynamic and thermodynamic variability has been observed. We address how the marine atmospheric boundary layer (MABL) in a trade-wind region adapts to fast and spatially varying sea-surface temperature (SST) structures, with a focus on changes in behaviour as a function of spatial scales. High-resolution atmospheric simulation data indicate that, at scales smaller than 1000 km, the effects of enhanced entrainment of dry free tropospheric air overcome those of surface evaporation over warm SST anomalies. This is supported by computations from a conceptual bulk model, which confirm two different responses in MABL temperature and specific humidity: an increase in the forcing SST warms the MABL and reduces its humidity content slightly. Locally, this behaviour suppresses the surface sensible heat flux (SHF) and enhances the surface latent heat flux (LHF), as observed recently with in situ, satellite, and numerical modelling data. At larger scales, instead, the MABL is more in equilibrium with the ocean surface and the sensitivity of turbulent fluxes to the underlying SST anomalies is significantly smaller. The scale dependence of the LHF variability is analysed with a linear scale decomposition method. SST is found to be the primary driver of LHF variability when scales smaller than about 1000 km are resolved, whereas atmospheric variability takes the lead for larger scales. Despite the effects on the mean LHF being small, the link between SST and LHF variability potentially has important implications for atmospheric shallow mesoscale circulations, which remain to be explored.

KEYWORDS

air–sea interactions, bulk model, entrainment, numerical simulation, sea-surface temperature, surface turbulent fluxes, trade winds

1 | INTRODUCTION

Energy exchanges between the ocean and the atmosphere affect the entire Earth system, with impacts on weather phenomena and climatic modes of variability (Seo *et al.*, 2023; Small *et al.*, 2008). Sea-surface temperature (SST) plays a fundamental role in shaping the atmospheric dynamics within the marine atmospheric boundary layer (MABL: e.g., Desbiolles *et al.*, 2021) and beyond it, with impacts on the whole troposphere (Li & Carbone, 2012). In particular, persistent, strong and large-scale SST gradients, such as those associated with western boundary currents (WBCs), are known to impact climatological rainfall and cloud cover (Minobe *et al.*, 2008; Njouodo *et al.*, 2018) as well as the evolution of synoptic storms (Hirata *et al.*, 2019; Parfitt *et al.*, 2016). Other than over WBCs, SST spatial variability has been linked with the modulation of clouds in a variety of dynamical regimes including over Southern Ocean eddies (Frenger *et al.*, 2013), in fronts and filaments in the Mediterranean Sea (Desbiolles *et al.*, 2021), as well as in the tropical ocean (Chen *et al.*, 2023). In this region, in particular, the role of SST and its spatial variability in modulating shallow mesoscale circulations (George *et al.*, 2023) and cloud mesoscale aggregation (Bony *et al.*, 2020) is still not completely understood. However, as low-level atmospheric mixing (Sherwood *et al.*, 2014) and low-level clouds (Bony *et al.*, 2015; Zelinka *et al.*, 2020) are among the major sources of uncertainties in global climate models, there is an urgent need to constrain the MABL dynamics and its links with the upper ocean better.

In the last decades, sea-surface features have been observed to take on a wide variety of shapes, which develop at scales of the order of $\mathcal{O}(100\,\text{km})$ and below (McWilliams, 2016), the so-called meso- and submesoscales. A recent quantification of energy spectra of the global oceans has revealed that spatial scales between 100 and 500 km (the lower range of mesoscales) explain more than 50% of the total energy resolved by modern observations (Storer *et al.*, 2022). With such high energy content, mesoscales contribute drastically to tightening air–sea interactions by forcing local anomalies in the redistribution of heat and buoyancy in both geophysical fluids (Bian *et al.*, 2023; Bishop *et al.*, 2020). Air–sea interactions, however, show a distinct dependence on the spatial scales considered. Chelton and Xie (2010) and Gentemann *et al.* (2020) highlight how, at scales larger than 1000 km, a negative correlation is observed between wind and SST, with the upper ocean responding to positive anomalies of surface wind with cooling. At mesoscales, instead, a positive correlation between wind and SST is observed, because of a modulation of atmospheric mixing by SST spatial variability that accelerates the surface wind over warm SST (Chelton *et al.*, 2004), with a mechanism that is known as vertical momentum mixing (VMM: Hayes *et al.*, 1989; Wallace *et al.*, 1989). Further detailed investigations on the role of submesoscale SST variability have, therefore, revealed that certain mechanisms, such as fine-scale oceanic frontogenesis, induce competing effects in the atmospheric response which feed back negatively on the mesoscale MABL adjustment processes (Conejero *et al.*, 2025; Renault *et al.*, 2024).

Recent work on high-resolution coupled climate models (Busecke *et al.*, 2025; Fernández *et al.*, 2025) has addressed the impact of fine-scale variability in the computation of large-scale surface turbulent heat fluxes. Busecke *et al.* (2025), in particular, identified a spatially varying contribution to air–sea surface heat exchanges due to SST, driving either local cooling or warming of the ocean, and a more uniform contribution by wind speed, which promotes sensible and latent heat fluxes from the ocean to the atmosphere. Overall, the two processes generate an upscaling effect of fine-scale structures on energy exchange, especially where SST gradients are strong, as in WBCs. Their dependence on the spatial scales of variability is expected, based on the scale-dependent behaviour of wind–SST and surface humidity–SST coupling recently identified in the northwestern tropical Atlantic (Fernández *et al.*, 2023), where the ElUcidating the RolE of Cloud–Circulation Coupling in ClimAte (EUREC^{4}A) field campaign took place in 2020 (Stevens *et al.*, 2021). In this region, at scales of $\mathcal{O}(100\,\text{km})$, the SST spatial variability has been found to force the overlying atmosphere in terms of stability (Borgnino *et al.*, 2025), increasing the atmospheric mixing over positive SST local anomalies. This is responsible for a net export of humidity out of the boundary layer, with an increase in low-level cloudiness, as demonstrated by in situ (Acquistapace *et al.*, 2022) and remote sensing (Chen *et al.*, 2023) data, and a strengthening of the surface evaporation because of the corresponding entrainment of dry air in the MABL (Borgnino *et al.*, 2025; Storer *et al.*, 2025). We name this process vertical water mixing (VWM), as it involves the modulation of surface humidity properties in a way that is reminiscent of the VMM mechanism. The dependence of this process on spatial scales of SST variability remains to be explored.

The turbulent nature of atmospheric boundary layers and the complexity of their dynamics calls for a simplified representation of their processes in order to gain an improved physical understanding of their evolution. Bulk models have been developed to achieve such a goal, especially in the trade-wind dynamical regime (e.g., Neggers *et al.*, 2006; Stevens *et al.*, 2002). They often rely on similarity theory for turbulent parametric closures and hypothesize a well-mixed layer where all information is contained in depth-averaged dynamic and thermodynamic quantities: in this way, the effect of each process at play may be isolated at ease. Investigating MABL dynamics through conceptual boundary-layer schemes has largely been proven useful in the literature. For example, Stevens *et al.* (2002) demonstrated that the explicit addition of fluxes of entrained momentum allowed us to reconstruct the wind climatology in tropical trade-wind regions. Significant conclusions on convective behaviour were reached as well, and specific mechanisms were first identified in the analysis of bulk models, such as the cumulus-valve mechanism (Neggers *et al.*, 2006; Vogel *et al.*, 2020).

In a context of growing interest in the emergence of shallow mesoscale circulations in trade-wind regions (George *et al.*, 2023), Naumann *et al.* (2019) illustrated that such simplified boundary-layer models could reproduce features of shallow convection arising from gradients in both radiative cooling and SST: above all, they highlighted the fact that the intensity of such motions is insensitive to the magnitude of gradients in boundary-layer radiative cooling, whereas it increases with increasing difference in SST values. Additionally, they underlined the pivotal role of moisture within the boundary layer to drive stronger entrainment fluxes compared with a dry boundary layer. However, a systematic characterization of the dependence of the bulk-model equilibrium solution on the underlying SST value is lacking. Moreover, the spatial scales of motion at which a bulk model is reliable and representative are yet to be identified.

In this work, we focus on the EUREC^{4}A region. The importance of this study area lies in the fact that the dynamics of shallow cumuli here are representative of the entire subtropical band (Medeiros & Nuijens, 2016). Thus, a characterisation of the physical processes that control the MABL response to SST can contribute to a step forward in our understanding of low-level clouds over a wide area of the global ocean. The scale dependence of the MABL–SST coupling is investigated, with a focus on the role of the VMM and VWM mechanisms. We do so by exploiting both a fully compressible three-dimensional realistic numerical simulation and a new MABL bulk model. Then, we study how the MABL dynamical and thermodynamical response impacts the surface turbulent latent heat flux, in terms of its mean and spatial variability. The theoretical background and the numerical experiments in use are presented in Section 2. Results on the MABL–SST scale dependence are illustrated in Section 3.1, whereas their impacts on the mean and spatial variability of the surface latent heat flux are presented in Section 3.2. Finally, Section 4 provides some discussion and future perspectives.

2 | DATA AND METHODS

2.1 | Full physics three-dimensional atmospheric simulation

A high-resolution atmospheric numerical simulation is performed with the Weather Research and Forecasting (WRF) model V4.1.5 (Skamarock *et al.*, 2019) with 3-km grid spacing and 75 vertical levels, 25 of which are below the average level of 800 hPa. Tropical trade-wind regions are characterized by insisting on wind-driven oceanic mixing, which tends to limit the sub-daily SST cycle and justifies the use of daily SST maps to force the model. Thus, daily maps of SST from the Multiscale Ultra-high Resolution (MUR) L4 analysis (Chin *et al.*, 2017), which provides realistic fine-scale SST structures at 1-km grid spacing, are applied as lower boundary conditions. Surface ocean currents are not accounted for. The simulation is run with atmospheric boundary conditions obtained from the European Centre for Medium-Range Weather Forecasts (ECMWF) Reanalysis Version 5 (ERA5: Hersbach *et al.*, 2020) and is representative of the EUREC^{4}A field campaign period (January–February 2020). The analyses are performed on data from February 2020 only. Model validation has been performed by Tartaglione *et al.* (2024) and Borgnino *et al.* (2025) in terms of the daily cycle of low-level clouds and vertical profiles of several atmospheric properties. In the same articles, all other technical details of the numerical simulation may also be found. Parameterization schemes used in the numerical simulation include the Yonsei Planetary Boundary Layer (Hong *et al.*, 2004) and the Revised Mesoscale Model 5 (MM5) surface-layer scheme (Jiménez *et al.*, 2012). We select offshore data at least 15 km away from land, so as to minimize breeze-like signals. Additionally, we neglect areas within approximately 150 km of the northern and western model boundaries due to marked model boundary effects: effectively, the outlined region spans from 0°–17°N and from 60°W–51°W (Figure 1).

2.2 | A low-complexity approach: A dynamic and thermodynamic bulk model

By leveraging existing bulk models for trade-wind regions, we merge the description of the MABL thermodynamics by Neggers *et al.* (2006) with the MABL-averaged horizontal momentum equations of Stevens *et al.* (2002). This results in a set of five prognostic ordinary differential equations, which converge stably to equilibrium solutions within a given range of boundary conditions.

The bulk model hypothesizes a well-mixed boundary layer, with thickness denoted by h, topped by a

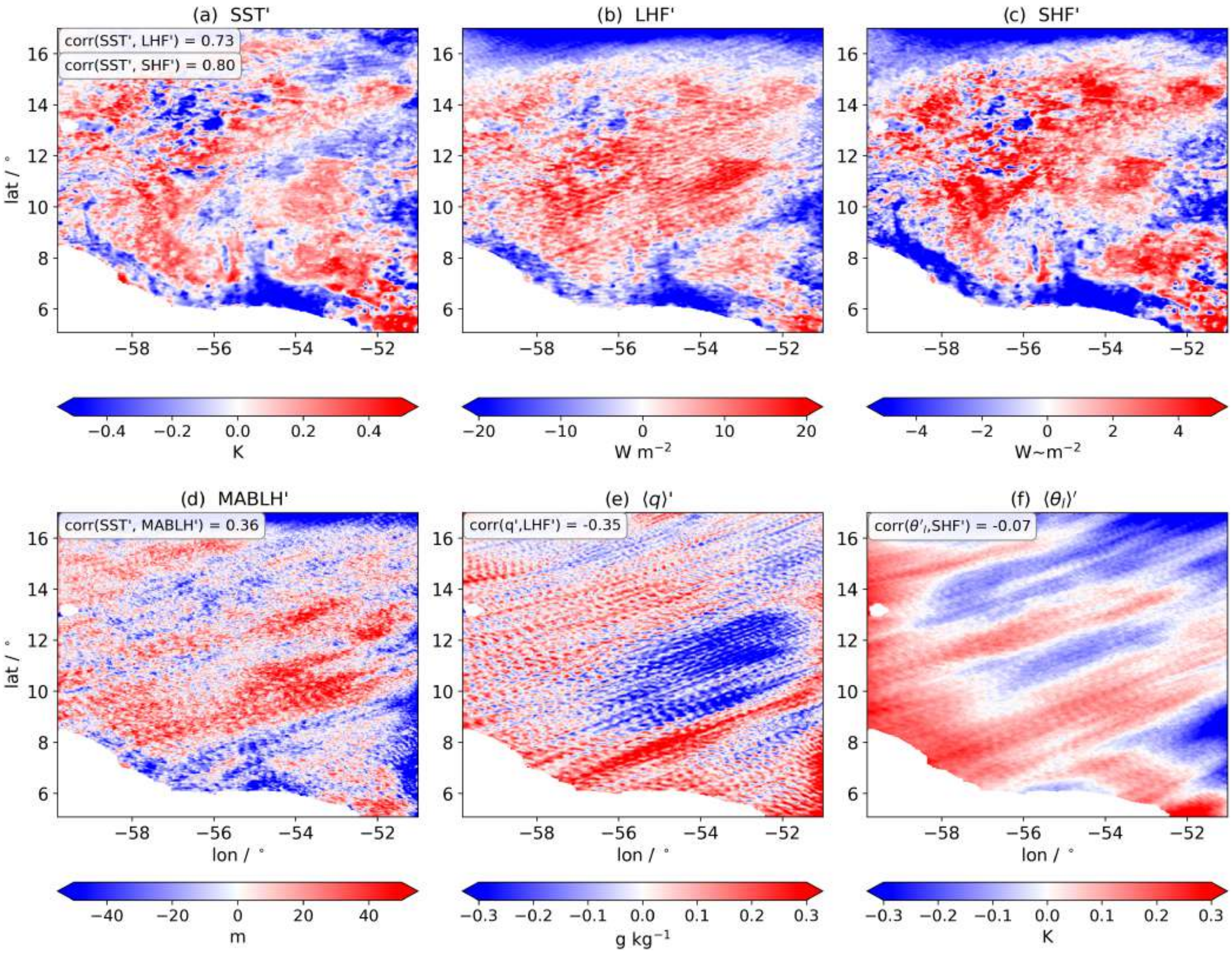

FIGURE 1 Spatial anomalies (as defined in Equation 1) of (a) SST, (b) surface bulk LHF, (c) surface bulk SHF, (d) MABL height h, (e) average water-vapour mixing ratio within the MABL $\langle q \rangle$, and (f) average MABL liquid water potential temperature $\langle \theta_l \rangle$, as output by the model computations for the February 1, 2020. The standard deviation of the Gaussian kernel was set to 150 km, corresponding to a scale of about 600 km. LHF and SHF were reconstructed through the application of the bulk formulae, as in Equations (2) and (3). Text boxes report the linear correlations between the fields indicated in brackets. [Colour figure can be viewed at wileyonlinelibrary.com]

conditionally unstable cloud layer. The vertically uniform distribution of liquid water potential temperature θ_l and total mixing ratio q_t within the mixed layer undergoes a jump accounting for the inversion at the transition layer, situated between the mixed-layer top and the cloud-base height. The free troposphere above the cloud layer, with variables denoted by a superscript $^+$, therefore provides a fixed boundary in terms of liquid water potential temperature, total mixing ratio, and geostrophic wind velocities (namely θ_l^+, q_t^+, U^+, and V^+, where U and V indicate the eastward and northward wind components).

The full set of equations that compose the model is reported in Appendix A, together with its validation with ERA5 data, performed following the approach by Neggers *et al.* (2006). Table 1 contains the boundary conditions used to compute the reference equilibrium solution of the bulk model. They are the spatial averages of the corresponding terms of the high-resolution WRF numerical simulation described above, averaged over the month of February 2020. As we are interested in the dependence of the MABL state on SST, we highlight that SST enters the system as a boundary condition that controls the surface sensible and latent heat fluxes. These, in turn, affect the entrainment of all variables, resulting in a nonlinear behaviour that is the object of the present study.

2.3 | Scale separation

We consider a scale-based decomposition on the WRF simulation data such that each field of interest ψ consists of

TABLE 1 Model fixed boundary conditions for the reference bulk model solution, taken as appropriate averages of the WRF numerical simulation.

Variable	Description	Value and units
SST	Sea-surface temperature	299.8 K
D	Large-scale divergence (avg. 1000–900 hPa)	3.6×10^{-6} s^{-1}
q^+	Specific humidity at 820 hPa	4.6×10^{-3} kg·kg^{-1}
θ_l^+	Liquid water potential temperature at 820 hPa	305.16 K
U^+	Zonal wind at 900 hPa	−9.4 m·s^{-1}
V^+	Meridional wind at 900 hPa	−3.3 m·s^{-1}
$F_{\text{adv},Q}$	Advective forcing of specific humidity	−0.6 g·kg^{-1} ·day^{-1}
F_{adv,θ_l}	Advective forcing of l.w. potential temperature	−1.1 K · day^{-1}
$F_{\text{adv}U}$	Zonal wind advective tendency	0.0 m · s^{-2}
$F_{\text{adv}V}$	Meridional wind advective tendency	0.0 m · s^{-2}
F_{rad}	Radiative cooling	−2 K · day^{-1}

large-scale, $\overline{\psi}$, and small-scale, ψ', components, mathematically

$$\psi = \overline{\psi} + \psi', \tag{1}$$

where the low-pass component $\overline{\psi}$ is obtained with an isotropic Gaussian kernel, the standard deviation σ of which sets the reference length-scale of separation. The Gaussian kernel is symmetric in the meridional and zonal directions, set to zero at distances larger than 3σ, and defined only on ocean grid points. We define the filter scale to be $L = 4\sigma$, as it corresponds to the domain in which the area under the Gaussian curve is about 95% of the total area. It is also verified that using a square boxcar filter with size L yields similar results (not shown), supporting that this is the physically relevant length-scale. A Gaussian filter is preferred with respect to a boxcar one, because it gives smoother results and reduces artifacts in spectral space. The high-pass component ψ' is what we will be referring to as a spatial anomaly, and it is typically one order of magnitude smaller than the respective low-pass variable.

Spatial anomalies of oceanic and atmospheric variables show distinct patterns of variability. With reference to the snapshots from the simulated day of February 1, 2020 (Figure 1), SST′ looks rather isotropic, whereas the MABL-averaged potential temperature $\langle\theta_l\rangle$ and humidity $\langle q\rangle$ are characterized by structures that are elongated in the direction of the surface wind (from northeast to southwest: Figure 1a,f,e, respectively). Note that angled brackets denote vertical averages within the MABL. Surface turbulent fluxes, latent heat flux (LHF) and sensible heat flux (SHF), being a product of ocean and atmospheric variables, display a spatial variability that has both oceanic and atmospheric features: appreciate, for instance, the widespread positive correlation of such surface turbulent fluxes with SST′ (Figure 1a). SHF is a source term for the MABL-mean liquid water potential temperature $\langle\theta_l\rangle$, even if straightforward links between the two may not be distinguished well visually here due to fast atmospheric variability in $\langle\theta_l\rangle$. Nonetheless, it may be observed that warm SST anomalies very often correspond to higher-than-average, drier, and warmer MABL columns (Figure 1d,e,f): the co-location of such anomalies with those of LHF is a crucial point for the rest of the discussion.

This qualitative link between thermodynamic variables and surface turbulent heat fluxes emerges more clearly from the flux bulk formulae, which we exploit to quantify how the small scales shape the spatial variability of the heat fluxes, with special attention to the role of SST. The bulk formulae read

$$\text{SHF} = \rho_a c_p C_h \langle U\rangle (SST - \langle\theta_l\rangle), \tag{2}$$

$$\text{LHF} = \rho_a L_v C_e \langle U\rangle [q^*(SST) - \langle q\rangle], \tag{3}$$

where $\rho_a = 1.2$ kg · m^{-3} is the air density, $c_p = 1004$ J · kg^{-1} · K^{-1} the air specific heat at constant pressure, and $L_v = 2.5 \times 10^6$ J · kg^{-1} the latent heat of vaporization: so as to simplify the analyses in terms of scale dependence, we assumed these coefficients to be uniform and constant; the saturation water-vapour mixing ratio q^* is a function of temperature only, as the surface pressure is kept fixed to a reference representative value of 1013 hPa. The established formulations of surface turbulent fluxes are generally making use of the surface atmospheric temperature and water-vapour mixing ratio. Here, so as to draw a consistent correspondence between the bulk model physics and the fully 3D simulation, our bulk reconstructions involve MABL-averaged thermodynamic variables, liquid water potential temperature θ_l, and humidity mixing ratio q. As clouds in our simulations lie above the computed MABL top, θ_l coincides with potential temperature; the latter, then, has the same variability of absolute air temperature at the surface, given that the MABL remains well-mixed in the daily averages: hence, the usage of θ_l is well justified here. Moreover, note that the coefficients used in the bulk formulae are inherited from the bulk model, which, by definition, is based on vertically integrated quantities.

As LHF is driven primarily by the specific humidity vertical difference at the air–sea interface, $q^*(SST) - \langle q\rangle$, it has a nonlinear dependence on SST through the Clausius–Clapeyron scaling.

We can thus define $\beta_h = \rho_a c_p C_h$ and $\beta_e = \rho_a L_v C_e$, in such a way that the fluxes become $\mathrm{SHF} = \beta_h \langle U\rangle (SST - \langle \theta_l\rangle)$ and $\mathrm{LHF} = \beta_e \langle U\rangle [q^*(SST) - \langle q\rangle]$. Using the scale separation defined in Equation (1), then, the fluxes can be written as

$$\begin{aligned} \mathrm{SHF} &= \beta_h \overline{\langle U\rangle}(\overline{\mathrm{SST}} - \overline{\langle \theta_l\rangle}) + \gamma_{\langle U\rangle}\langle U\rangle' \\ &\quad + \gamma_{\mathrm{SST}}\mathrm{SST}' + \gamma_{\langle \theta_l\rangle}\langle \theta_l\rangle' + O'', \end{aligned} \tag{4}$$

$$\begin{aligned} \mathrm{LHF} &= \beta_e \overline{\langle U\rangle}[q^*(\overline{\mathrm{SST}}) - \overline{\langle q\rangle}] + \lambda_{\langle U\rangle}\langle U\rangle' \\ &\quad + \lambda_{\mathrm{SST}}\mathrm{SST}' + \lambda_{\langle q\rangle}\langle q\rangle' + O'', \end{aligned} \tag{5}$$

where the γ and the λ functions are the product of relevant low-pass fields, as detailed in Appendix A.1 of the Appendix; O'' indicates the terms containing the product of two spatial anomaly fields, which are much smaller than the others and can be neglected.

Let $\mathrm{SHF^c}$ and $\mathrm{LHF^c}$ be the fluxes computed with the low-pass filtered fields, which can be interpreted as the surface fluxes of a coarse numerical model, namely

$$\mathrm{SHF^c} = \beta_h \overline{\langle U\rangle}(\overline{\mathrm{SST}} - \overline{\langle \theta_l\rangle}), \tag{6}$$

$$\mathrm{LHF^c} = \beta_e \overline{\langle U\rangle}[q^*(\overline{\mathrm{SST}}) - \overline{\langle q\rangle}]. \tag{7}$$

The differences $\mathrm{SHF} - \mathrm{SHF^c}$ and $\mathrm{LHF} - \mathrm{LHF^c}$ thus represent the fine-scale structure of the missing flux in a coarse model and are given by the γ and λ terms in the above equations. Following Busecke *et al.* (2025), their filtered versions quantify the small-scale contribution to the large-scale fluxes in a coarse model that has no small-scale variability, namely

$$\begin{aligned} \mathrm{SHF}^* &= \overline{\mathrm{SHF}} - \overline{\mathrm{SHF}}^c = \beta_h \overline{\langle U\rangle(\mathrm{SST} - \langle \theta_l\rangle)} \\ &\quad - \beta_h \overline{\overline{\langle U\rangle}(\overline{\mathrm{SST}} - \overline{\langle \theta_l\rangle})} \\ &= \overline{\gamma_{\langle U\rangle}\langle U\rangle'} + \overline{\gamma_{\mathrm{SST}}\mathrm{SST}'} + \overline{\gamma_{\langle \theta_l\rangle}\langle \theta_l\rangle'} + \overline{O''}, \end{aligned} \tag{8}$$

$$\begin{aligned} \mathrm{LHF}^* &= \overline{\mathrm{LHF}} - \overline{\mathrm{LHF}}^c = \beta_e \overline{\langle U\rangle[q^*(\mathrm{SST}) - \langle q\rangle]} \\ &\quad - \beta_e \overline{\overline{\langle U\rangle}[q^*(\overline{\mathrm{SST}}) - \overline{\langle q\rangle}]} \\ &= \overline{\lambda_{\langle U\rangle}\langle U\rangle'} + \overline{\lambda_{\mathrm{SST}}\mathrm{SST}'} + \overline{\lambda_{\langle q\rangle}\langle q\rangle'} + \overline{O''}. \end{aligned} \tag{9}$$

This linear formulation reduces complexity and allows us to look into scale-dependent interactions among the variables of interest: by adopting the Gaussian filter introduced above as the reference integral kernel, we define local statistics as follows. Given a generic field ψ, its local mean value is $\overline{\psi}$, as defined above. Its local variance, then, is $\overline{\psi'^2}$, and its local covariance with another field ϕ is $\overline{\psi'\phi'}$. The advantage of these local spatial statistics is that they compute an expectation value by weighting neighbouring points with the Gaussian kernel, the extent of which scales with the filter scale L.

Another metric that is commonly used in air–sea interaction studies (e.g., Seo *et al.*, 2023) is the coupling coefficient α_ψ, which is defined here to be the least-squares linear slope between the spatial anomalies of a given field ψ with respect to the spatial anomalies of the SST, such that

$$\psi' = \alpha_\psi\, SST' + \psi'_{\mathrm{atm}}, \tag{10}$$

with ψ'_{atm} indicating the residuals of the least-squares computation. These residuals are statistically independent from the SST and are meant to represent the atmospheric variability only. Physically, this indicates that the coupling coefficient gives an estimate of the strength of coupling with the SST and, in what follows, this is also called the sensitivity of ψ to SST.

Within this framework, we can also compute a closed budget of the spatial variance of LHF, accounting for the variances and covariances of SST, MABL humidity, and wind-speed anomalies, defined with the Gaussian filter. Namely,

$$\begin{aligned} \overline{\mathrm{LHF}'^2} &= \lambda^2_{\langle U\rangle}\overline{\langle U\rangle'^2} + \lambda^2_{\langle q\rangle}\overline{\langle q\rangle'^2} + \lambda^2_{\mathrm{SST}}\overline{\mathrm{SST}'^2} \\ &\quad + 2\lambda_{\langle U\rangle}\lambda_{\langle q\rangle}\overline{\langle U\rangle'\langle q\rangle'} \\ &\quad + 2\lambda_{\langle U\rangle}\lambda_{\mathrm{SST}}\overline{\langle U\rangle'\mathrm{SST}'} + 2\lambda_{\mathrm{SST}}\lambda_{\langle q\rangle}\overline{\mathrm{SST}'\langle q\rangle'}. \end{aligned} \tag{11}$$

By exploiting the statistical decomposition of ψ' involving the coupling coefficients (Equation 10), this can be used to separate properly the oceanic and atmospheric terms that control the variability of LHF, which gives

$$\begin{aligned} \overline{\mathrm{LHF}'^2} &= \lambda^2_{\langle U\rangle}\overline{\langle U\rangle'^2_{\mathrm{atm}}} + \lambda^2_{\langle q\rangle}\overline{\langle q\rangle'^2_{\mathrm{atm}}} \\ &\quad + 2\lambda_{\langle U\rangle}\lambda_{\langle q\rangle}\overline{\langle U\rangle'_{\mathrm{atm}}\langle q\rangle'_{\mathrm{atm}}} \\ &\quad + \left(\lambda_{\mathrm{SST}} + \alpha_U\lambda_{\langle U\rangle} + \alpha_q\lambda_{\langle q\rangle}\right)^2\overline{\mathrm{SST}'^2}. \end{aligned} \tag{12}$$

3 | RESULTS

3.1 | Scale dependence of the MABL–SST coupling

To explore the scale-dependence of air–sea coupling, we analyse daily averaged fields from the realistic WRF simulation over the EUREC^{4}A region, validated in Tartaglione *et al.* (2024) and Borgnino *et al.* (2025). Using the WRF MABL height $\langle h\rangle$, the definition of which is based on the critical Richardson number, we compute the coupling coefficients of the MABL averaged liquid water potential

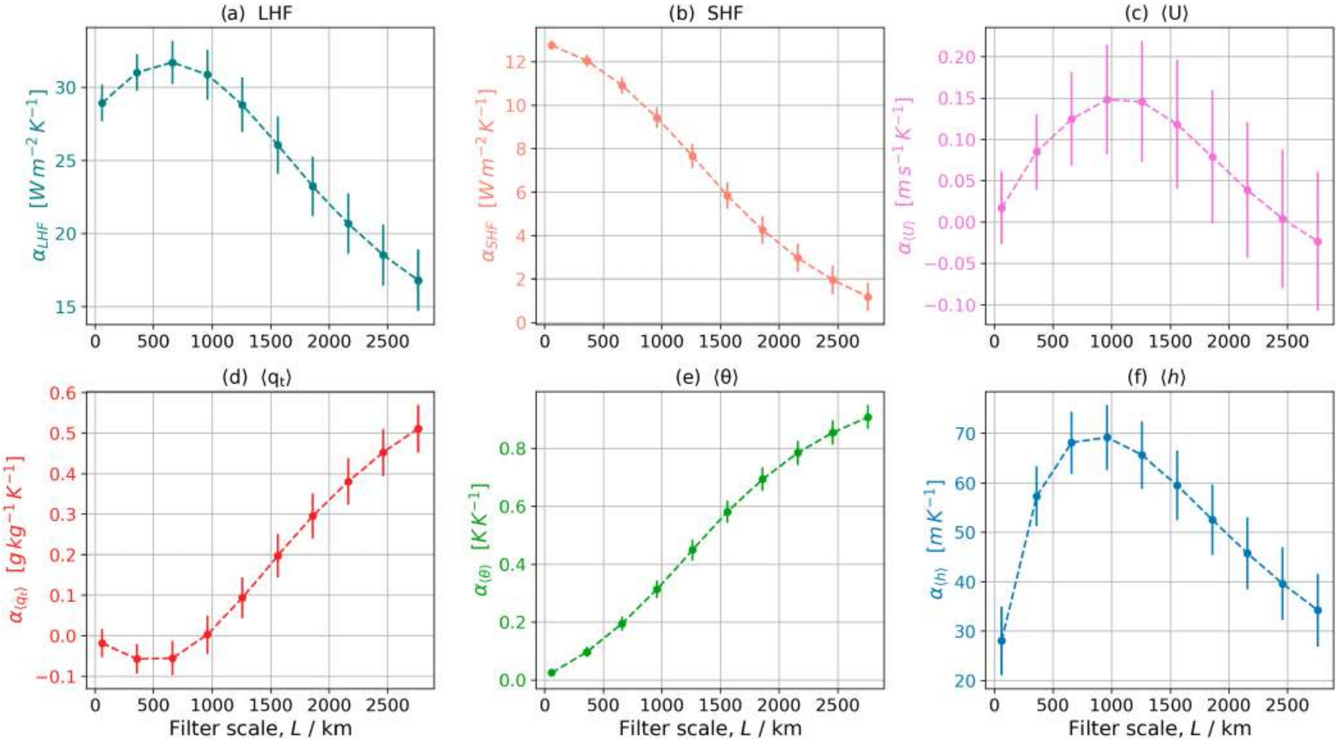

FIGURE 2 Coupling coefficients for different atmospheric variables as a function of the filter scale L. [Colour figure can be viewed at wileyonlinelibrary.com]

temperature $\langle \theta_l \rangle$ and specific humidity $\langle q \rangle$. The liquid water fraction in $\langle q_t \rangle$ is negligible with respect to water vapour $\langle q \rangle$ and will not be presented in the following, as most clouds lie above the MABL.

Coupling coefficients are computed for the spatial anomalies of $\langle h \rangle$, $\langle \theta_l \rangle$ and $\langle q \rangle$, LHF, SHF, and $\langle U \rangle$ with respect to SST for different values of filter scale L in the range 60–3000 km (Figure 2).

MABL height displays a positive coupling with SST′ for the entire range of scales explored, with the maximum value at about 800 km (Figure 2f). MABL-averaged liquid water potential temperature $\langle \theta_l \rangle$ shows an increasing value of coupling with SST′ for increasing L, whereas MABL-averaged specific humidity $\langle q \rangle$ has a negative coupling for scales smaller than 1000 km and a positive coupling for larger scales (Figure 2e,d, respectively). This result is in line with observational and modelling studies in the same area (Acquistapace *et al.*, 2022; Borgnino *et al.*, 2025; Fernández *et al.*, 2023). In particular, it is interesting to highlight that a negative $\alpha_{\langle q \rangle}$ indicates that the MABL drying associated with enhanced entrainment over warmer SST dominates over the MABL moistening due to increased surface evaporation, and is a signature of the VWM mechanism. At large scales, the positive value of $\alpha_{\langle q \rangle}$ suggests that surface evaporation becomes the dominant process, leading to an increase in MABL humidity with SST. In this regime, specific humidity rises with SST at a rate that tends to that predicted by the Clausius–Clapeyron relation (approximately 1.3 $\text{g} \cdot \text{kg}^{-1} \cdot \text{K}^{-1}$), while both surface fluxes and entrainment weaken. The scale dependence of α_{LHF} (always positive with a maximum for $L =$ 600 km, Figure 2a) is consistent with that of $\alpha_{\langle q \rangle}$. This, as will be discussed further in the context of the bulk model dynamics, suggests that the variation of MABL humidity is directly responsible for the LHF coupling with SST.

In light of this analysis, we note that, as the free troposphere is drier and warmer than the MABL, the increased vertical mixing over warm SST anomalies can produce different responses in the two key thermodynamic MABL variables: at fine scales, potential temperature increases over warm SST while specific humidity decreases weakly.

We next exploit the bulk model to explore the processes at play with a minimal physics approach. Firstly, we discuss the equilibrium solution of the bulk model using as boundary conditions the average values obtained from the WRF numerical simulation, as indicated in Table 1. The initial conditions for the five prognostic variables are $h_0 = 500$ m, $q_{t0} = q_s^* - 5 \text{ g} \cdot \text{kg}^{-1} = 16.8 \text{ g} \cdot \text{kg}^{-1}$, $\theta_{l,0} = \theta_{l,s} - 3 \text{ K} = 295.7$ K, $U_0 = U^+ = -9.4 \text{ m} \cdot \text{s}^{-1}$, $V_0 = V^+ = -3.3 \text{ m} \cdot \text{s}^{-1}$. The wind components have been initialized to match the average free-tropospheric flow in geostrophic equilibrium at a latitude of 10°N, that is, the central latitude of the WRF simulation. The bulk model reaches an equilibrium in about 40 simulated hours

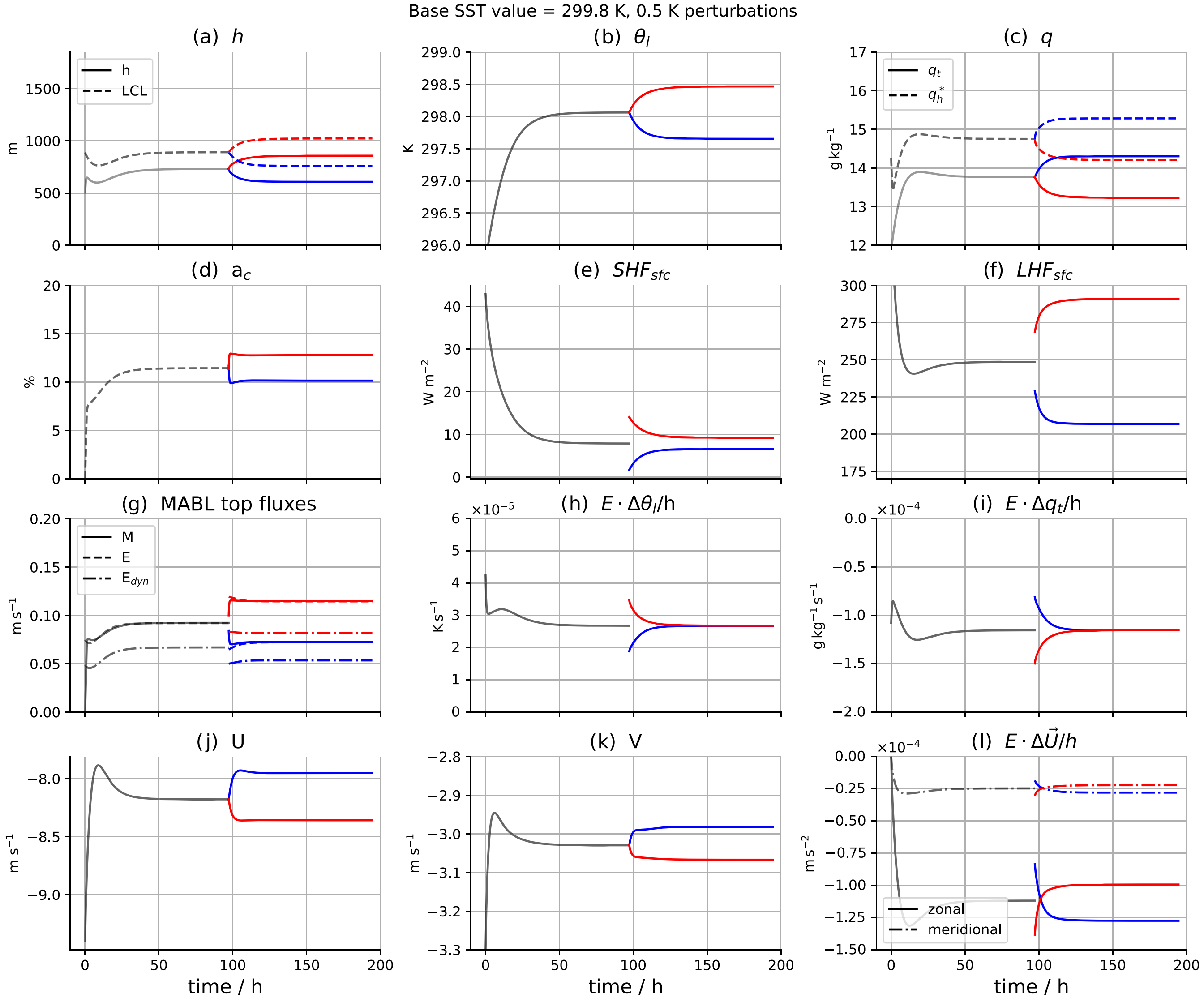

FIGURE 3 Time evolution of variables in the bulk model. Grey lines refer to relaxation towards the steady-state solution for SST = 299.8 K, to which an SST anomaly of 0.5 K is added (red lines) or removed (blue lines) and the subsequent time evolution shown. [Colour figure can be viewed at wileyonlinelibrary.com]

(grey lines in Figure 3). At equilibrium, the height of the mixed layer h is about 750 m (Figure 3a), which results from the balance between the convective mass flux M and the entrainment E (Figure 3g). The lifting condensation level (LCL, computed following Romps, 2017) sits higher than h in such a way that the convective area fraction a_c (which gives an approximate indication of cloud cover) is slightly larger than 10%. As expected, LHF (Figure 3f, full line) is much higher than SHF (Figure 3e), $\mathcal{O}(\text{LHF}) \sim 250\ \text{W} \cdot \text{m}^{-2} > \mathcal{O}(\text{SHF}) \sim 8\ \text{W} \cdot \text{m}^{-2}$.

If a perturbation of 0.5 K is added to or subtracted from the reference SST value, a new equilibrium is reached. In particular, the time evolution of variables depending directly on SST (such as the surface turbulent fluxes and the entrainment, which is a function of the surface buoyancy flux) naturally presents a jump discontinuity, whereas (most of) the variables that depend on the equilibrium among different processes display an exponential-like relaxation. We discuss in the following the response to a positive thermal anomaly (red curves in Figure 3) and note that the response to a negative one (blue curves) mostly mirrors it. A warmer surface promotes the growth of the MABL because of the sudden increase in entrainment, which is the only term that can make the MABL thicker. This growth is then balanced by an enhanced mass flux, which increases both thanks to a widening of the convective area fraction (Figure 3d) and because of an increase in the Deardorff vertical velocity (not shown). A warmer surface also increases the MABL liquid water potential temperature (Figure 3b), in such a

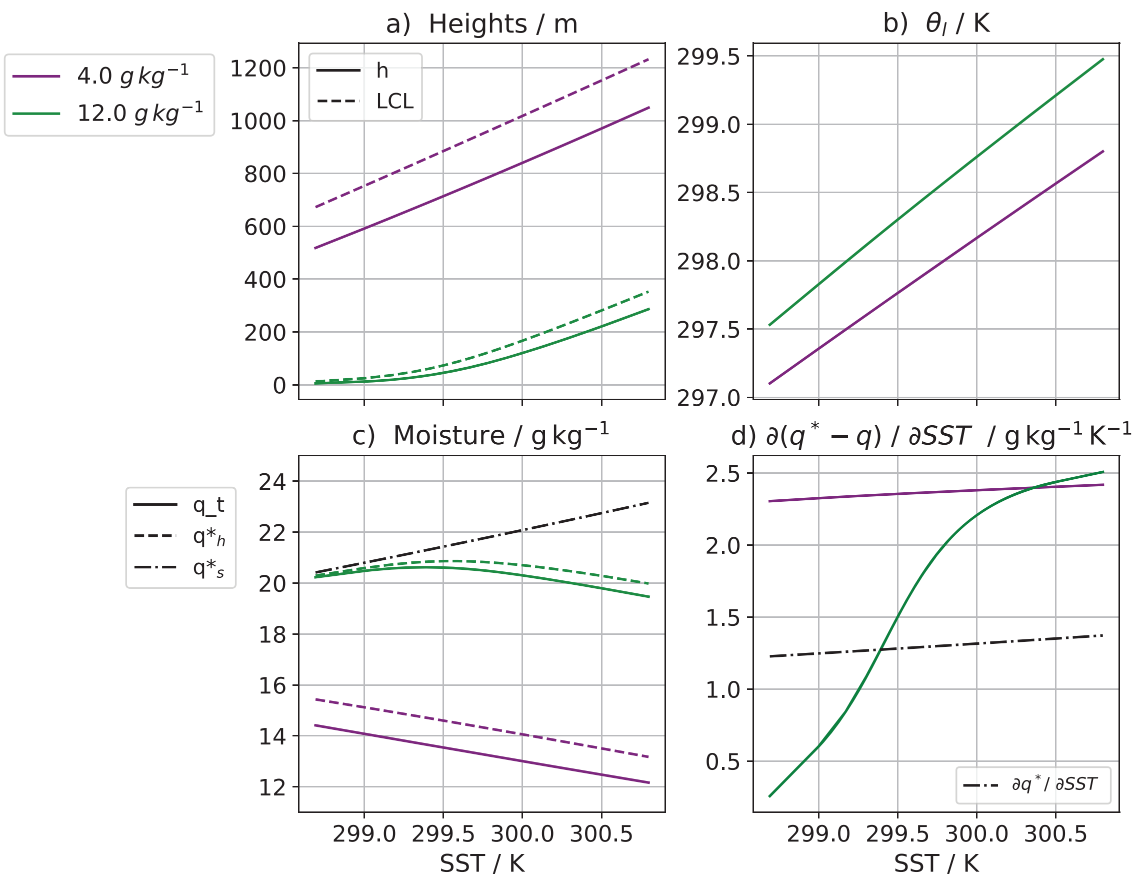

FIGURE 4 Equilibrium values from the bulk model of (a) LCL and mixed-layer height h, (b) liquid water potential temperature θ_{l}, (c) mixed-layer specific humidity q_{t}, top saturation q^*_{h}, and surface saturation q^*_{s}, and (d) derivative of the subsaturation with respect to SST, $\partial(q^* - q_{\mathrm{t}})/\ \partial SST$ (solid lines) and derivative of the saturation term only $\partial q^*/\partial SST$ (dot–dashed line). Two cases of free tropospheric specific humidity are compared, namely a realistic setup (4 g $\cdot$ kg^{-1}, purple lines) and an unrealistic, moister one (12 g $\cdot$ kg^{-1}, green lines). [Colour figure can be viewed at wileyonlinelibrary.com]

way that the perturbation in SHF fades out and relaxes back towards the initial base state value of roughly 8 W $\cdot$ m^{-2}. The increase of θ_{l} is supported not only by the surface flux but also by the entrainment of warmer air at the MABL top (Figure 3h, $E_{\theta_{\mathrm{l}}}$). Because of its vertical structure, specific humidity displays an opposite response, in line with the VWM mechanism described for scales smaller than 1000 km in the WRF simulations. The fact that the free tropospheric air is drier than the MABL means that the increased entrainment reduces MABL specific humidity (Figure 3c). This, together with an increased surface saturation specific humidity (because of the higher SST), makes the surface LHF stronger (Figure 3f).

A warmer and drier MABL necessarily displays a higher LCL (Figure 3a, dashed lines), which is again roughly 200 m higher than h. The height difference between LCL and h does not change appreciably with SST, because relative humidity at the top of the boundary layer (which depends on the ratio $q_{\mathrm{t}}/q^*_{\mathrm{h}}$) is nearly constant: MABL moisture is low whenever the MABL is thick and its top is thus cold. Despite this, the qualitative metric for cloud cover (a_{c}) suggests that over warmer SST there are more low-level clouds, which is in line with the in situ findings of Acquistapace *et al.* (2022). This, together with the fact that the dependence of MABL q_{t} and LHF as a function of SST coincides dynamically with the behaviour observed by Acquistapace *et al.* (2022) and Chen *et al.* (2023) and modelled by Borgnino *et al.* (2025) and Storer *et al.* (2025), indicates that the bulk model represents the key physical processes at play properly, in particular the VWM.

To strengthen the point that the presence of a dry free atmosphere above the MABL is key in leading to a net MABL drying with increasing SST, we next compute the equilibrium solutions as a function of SST with two different values of free tropospheric specific humidity, adding to the realistic scenario ($q_{\mathrm{t}}^+ = 4$ g $\cdot$ kg^{-1}) a very moist one ($q_{\mathrm{t}}^+ = 12$ g $\cdot$ kg^{-1}, Figure 4). As already discussed above, the reference case with $q_{\mathrm{t}}^+ = 4$ g $\cdot$ kg^{-1} displays a MABL behaviour that is consistent with the VWM mechanism: with increasing SST, the larger sensible heat flux (which dominates the buoyancy flux) implies a larger entrainment at the top of the MABL, making the boundary layer thicker and drier. The action of entrainment fluxes is twofold: (a) promoting the mixing of moist MABL air with dry free-tropospheric air and (b) moving mass physically, which deepens the MABL and dilutes the amount of water vapour. The numerical analysis of the dependence of the equilibrium water-vapour mixing ratio on SST demonstrates nonetheless that the contribution, in terms of sensitivity to SST, of the entrainment rate E is much larger than that of the variation of h (see Appendix A.3).

With the drying of the mixed layer, its moisture content diverges further from surface saturation levels (the full line detaches from the dash–dotted one as SST increases, Figure 4c). Thus, the sensitivity of the air–sea moisture difference is strictly larger than the Clausius–Clapeyron scaling (Figure 4d). In formula form,

$$\frac{\partial\left(q_{\mathrm{s}}^{*}-q_{\mathrm{t}}\right)}{\partial SST}>\frac{\partial\, q_{\mathrm{s}}^{*}}{\partial SST}. \tag{13}$$

Entrainment, thus, reduces the specific and relative humidity of the mixed layer by adding mass to it, mixing, and warming it. In this way, it feeds back positively on the evaporative fluxes at the sea surface and contributes to extracting more energy from the sea.

If the free-tropospheric specific humidity is high (e.g., $q_{\mathrm{t}}^{+}=12\ \mathrm{g}\cdot\mathrm{kg}^{-1}$), the mixed-layer moisture content for SST < 299.4 K increases with SST at a rate lower than the Clausius–Clapeyron scaling (Figure 4c). In such circumstances, the entrainment feedback in boundary-layer humidity is not large enough to enhance the sensitivity of LHF to SST. The term $\partial(q_{\mathrm{s}}^{*}-q_{\mathrm{t}})/\partial SST$ is indeed smaller than $\partial q_{\mathrm{s}}^{*}/\partial SST$ (Figure 4d) for SST < 299.4 K. Nonetheless, the present model cannot sustain such a condition, as the mixed-layer height drops to unreasonably low values (Figure 4a). We argue that, since at equilibrium the radiative loss of energy per unit mass must be balanced by the θ_{l} fluxes at the surface and at the MABL top, in the presence of a moister free troposphere the MABL humidity content approaches the surface saturation value, hence keeping the surface fluxes very small: this, in turn, limits the entrainment fluxes. The low energy input into the boundary layer can only compensate for the radiative loss of a shallow mixed layer. The introduction of an interactive radiation scheme would be necessary to investigate this configuration further (see Zheng, 2019), but this goes beyond the goals of the present study.

Until now, we have discussed solutions of the bulk model at equilibrium. When considering an air mass advected over an SST anomaly, however, the residence time of the air over it might be too short for the system to reach equilibrium. For this reason, and to connect those results further to the realistic atmospheric simulation described above, we discuss the bulk model adjustment time-scales. Using exponential functions to fit the time evolution of q_{t}, θ_{l}, E, and h, we obtain the following e-folding time-scales: $\tau_{\theta_{\mathrm{l}}}\sim 7.6$–$8.9\ h$, $\tau_{q_{\mathrm{t}}}\sim 5.6$–$7.2\ h$, $\tau_{E}\sim 6.1\ h$, $\tau_{h}\sim 6.3$–$7.8\ h$. Considering that the plateau is reached within 3–5 e-folding times and using typical wind speeds in the Trades (5–10 $\mathrm{m\cdot s^{-1}}$), the bulk model indicates that the MABL can adjust fully to SST anomalies at spatial scales larger than 500 km (for low winds) to 1500 km (for high winds). At smaller scales, thermodynamical and dynamical inertia of the MABL allows only a partial adjustment. The fact that the WRF-derived coupling coefficients for MABL humidity and temperature tend to zero for decreasing filter scale below $L=600$ km supports this physical interpretation. Furthermore, the full adjustment of MABL temperature at large scales (where $\alpha_{\langle\theta_{\mathrm{l}}\rangle}$ tends to 1) implies a low sensitivity of SHF, and thus of entrainment, to SST. In this condition, boundary-layer moisture is only modified by surface fluxes and thus increases over warmer waters ($\alpha_{\langle q\rangle}>0$), as observed in WRF outputs at scales above 1000 km (see Figure 2d).

3.2 | Impacts on surface latent heat flux

The synergistic analysis of the high-resolution numerical simulations and the bulk model has highlighted that, at scales smaller than 1000 km, having a dry free troposphere, the enhanced vertical mixing over warm SST anomalies makes the MABL dryer in such a way that the surface latent heat flux is more sensitive to SST with respect to the pure Clausius–Clapeyron scaling. This explains the non-monotonic behaviour of α_{LHF} as a function of filter scale (Figure 2a) and indicates that the small-scale SST variability drives local changes in LHF that we now characterize in terms of spatial averages and variability.

The LHF coupling coefficient α_{LHF} suggests that, in the range of scales between 400 and 1000 km, a 1-K difference in the SST can lead to variations of LHF of more than 30 $\mathrm{W\cdot m^{-2}}$. This leads to large local relative differences of actual LHF with respect to the fluxes computed using coarse fields, LHF$^{\mathrm{c}}$. In particular, the relative differences increase as a function of filter scale and can reach values up to 30%–40% (as shown by the tails of the distributions in Figure 5a). The distributions of the upscaling effect of the small-scale variability on the large-scale latent heat flux LHF* also show a scale dependence (Figure 5b). In particular, we compute the percentage contribution of LHF* with respect to LHF$^{\mathrm{c}}$, for different scales of the Gaussian filter. The distributions shown in the figure are computed with respect to the spatial variability of the low-pass filtered fields, as well as the temporal variability across the

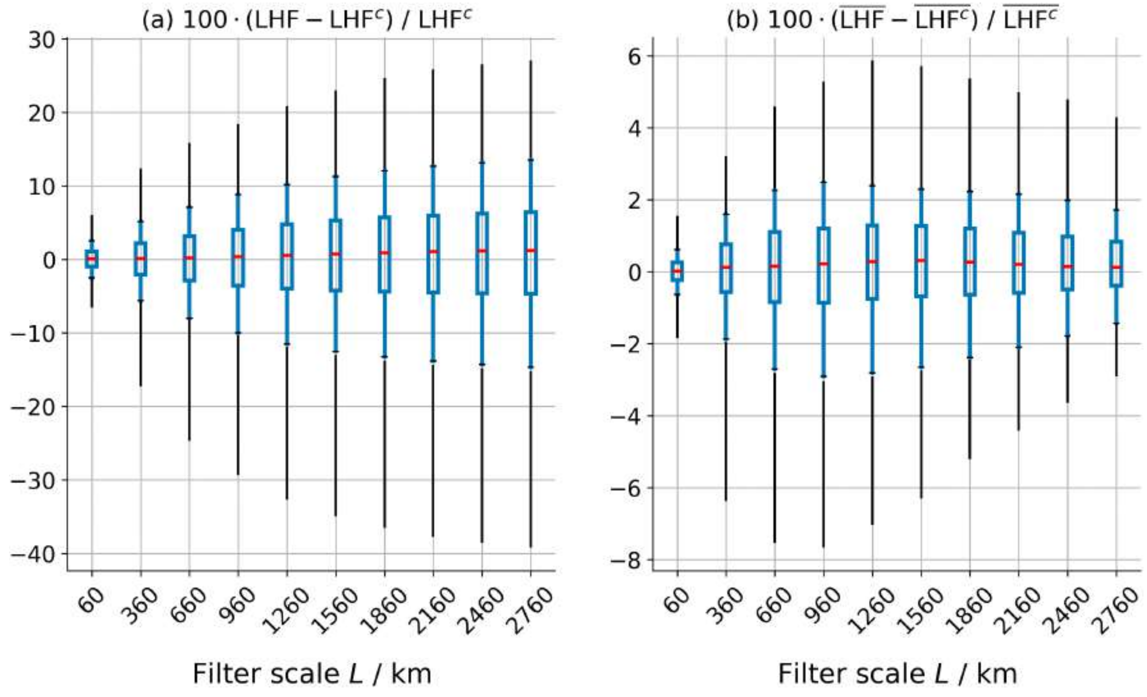

FIGURE 5 (a) Box plot of the percentage difference between the high-resolution LHF and LHF^c, as a function of filter scale. (b) Box plot of the upscaling effect of small-scale variability of LHF, expressed as a percentage ratio of LHF* and LHF^c, as a function of filter scale. [Colour figure can be viewed at wileyonlinelibrary.com]

month of February 2020. The 0.5th and the 99.5th percentiles, indicated by the whiskers, show that the largest values are in the range 700–1500 km. This indicates that the MABL dynamics at these scales have a net upscaling effect on the large-scale flux, at least in specific places and instants (Figure 5b). Overall, however, the median values are extremely low for all filter scales, and also the extreme values remain within 10% of the coarse LHF^c. This suggests that the SST variability, in this region, has a small contribution to the large-scale LHF, because SST gradients are small and thus the effects of positive and negative anomalies cancel out when filtering over larger scales.

Despite the small-scale variability of LHF not having a large impact on larger-scale averaged LHF, we show here that the small-scale SST variability is the main factor responsible for the small-scale LHF variance and has the potential to influence the lower atmospheric dynamics, as discussed below. By exploiting the scale separation introduced in Equation (1), we can explicitly compute the local variance of LHF in such a way that its budget is closed (Equations 11 and 14) and we can analyse all terms as a function of the filter scale L.

This decomposition may be recast in percentage terms by multiplying both sides by $100/\overline{\mathrm{LHF}'^2}$. With it, we can estimate the role of local variances of surface wind speed, SST, and low-level specific humidity, as well as their respective local covariances, in shaping the local variance of LHF. It is found that, for all scales considered, the SST variance term is the single term that contributes most to the LHF variance (Figure 6c). This term dominates because of the strong dependence of saturation specific humidity on SST (i.e., the Clausius–Clapeyron scaling) that is contained in the λ_{SST} function. The $\overline{\mathrm{SST}'\langle U\rangle'}$ term (Figure 6d), which is remapped onto the $\alpha_{\langle U\rangle}\overline{\mathrm{SST}'^2}$ term, also gives a positive contribution, with a peak in the range 400–1600 km. This term represents the VMM mechanism and is indicative of the action of MABL-top entrainment that accelerates the surface wind over warm SST mesoscale anomalies. In fact, the median of this term is different from zero for scales smaller than 2000 km. Similarly, we can identify the action of the VWM mechanism in the term that includes $\alpha_{\langle q\rangle}$ explicitly (Figure 6f) and gives a positive contribution for scales smaller than 1000 km and a negative contribution at larger scales. Note that the function λ_q is negative, meaning that the covariance of SST$'$ and $\langle q\rangle'$ is negative at small scales (drier MABL over warm SST) and becomes positive at large scales, which corresponds to the more equilibrated moistening of the MABL via enhanced evaporation over positive SST anomalies. This corresponds to VWM increasing the LHF variance at small scales with a link between the entrainment-driven MABL drying and the surface flux. For larger scales, instead, this term becomes negative, suggesting that a moister MABL over warm SST dampens LHF variability. Concerning terms that do not include SST, we see that the variance of specific humidity and wind speed

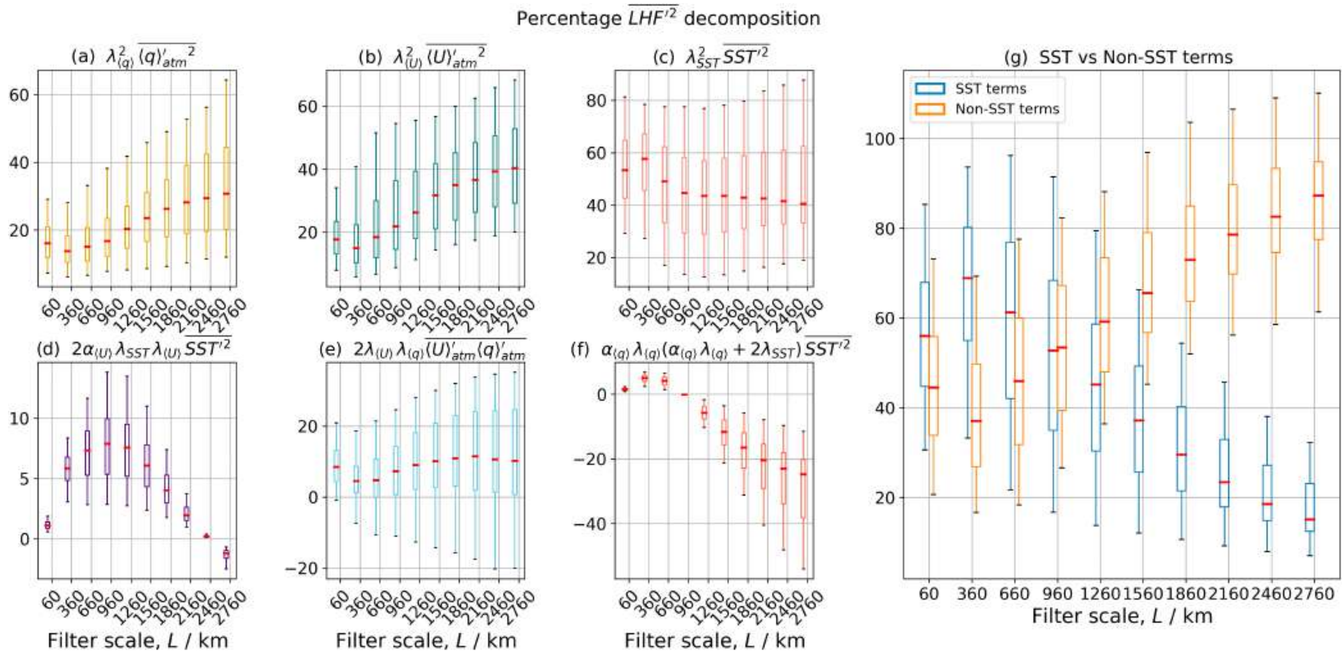

FIGURE 6 LHF variance decomposition: (a)–(f) display the ranges of variation of each term in Equation (14) as a function of the filter scale L. (g) summarizes the relative contributions of all terms depending on SST in Equation (14) (blue) and all other terms unrelated to SST (orange). All red segments represent the median of each distribution, boxes limit the interquartile range and whiskers include values between the 10th and 90th percentiles. [Colour figure can be viewed at wileyonlinelibrary.com]

(Figure 6a,b) gives a smaller contribution with respect to the SST alone, which increases with increasing spatial scales. Also, the $\overline{\langle U\rangle'_{\rm atm}\langle q\rangle'_{\rm atm}}$ covariance term increases slowly with increasing scale. As the terms $\alpha^2_{\langle U\rangle}\lambda^2_{\langle U\rangle}\overline{\rm SST'^2}$ and $2\alpha_{\langle U\rangle}\alpha_{\langle q\rangle}\lambda_{\langle U\rangle}\lambda_{\langle q\rangle}\overline{\rm SST'^2}$ contribute less than 1% at all scales (not shown), we neglect them in the decomposition of LHF variance, which can be written as

$$\begin{aligned}\overline{\rm LHF'^2} = {} & \lambda^2_{\langle U\rangle}\overline{\langle U\rangle'^2_{\rm atm}} + \lambda^2_{\langle q\rangle}\overline{\langle q\rangle'^2_{\rm atm}} \\ & + 2\lambda_{\langle U\rangle}\lambda_{\langle q\rangle}\overline{\langle U\rangle'_{\rm atm}\langle q\rangle'_{\rm atm}} \\ & + \underbrace{\lambda^2_{\rm SST}\overline{\rm SST'^2}}_{\text{Clausius-Clapeyron}} + \underbrace{2\alpha_{\langle U\rangle}\lambda_{\rm SST}\lambda_{\langle U\rangle}\overline{\rm SST'^2}}_{\text{VMM}}\end{aligned} \tag{14}$$

$$+ \underbrace{\alpha_{\langle q\rangle}\lambda_{\langle q\rangle}(\alpha_{\langle q\rangle}\lambda_{\langle q\rangle} + 2\lambda_{\rm SST})\overline{\rm SST'^2}}_{\text{VWM}}. \tag{15}$$

Overall, the SST terms dominate the LHF variance at scales smaller than 1000 km and the atmospheric terms dominate it at larger scales (Figure 6g). This can be interpreted using the fact that, typically, the autocorrelation length of oceanic fields is smaller with respect to the autocorrelation length of atmospheric variables. Thus, at small scales, atmospheric fields can be considered to be roughly constant and only the spatial variability of SST modulates the variability of turbulent fluxes. A visualization of this behaviour is shown in Appendix Figure A2, where SST′ and LHF′ fields are shown for different scales of the filter, for February 1, 2020. They clearly show that, for small σ, the SST′ and LHF′ structures are co-located.

4 | SUMMARY AND CONCLUSIONS

SST spatial variability in the Trades has recently been found to modulate the MABL dynamics in such a way that over warm water the MABL gets thicker and drier, enhancing surface evaporation and increasing the low-cloud cover thanks to a net export of humidity above the LCL (Acquistapace *et al.*, 2022; Borgnino *et al.*, 2025; Chen *et al.*, 2023; Storer *et al.*, 2025). This process, which we name here vertical water mixing (VWM), in parallel with the well-known vertical momentum mixing (VMM), has been interpreted with in situ data (Acquistapace *et al.*, 2022) and high-resolution numerical simulations (Borgnino *et al.*, 2025) as being dominated by the entrainment of dry air at the MABL top.

Using a linear scale separation method based on a Gaussian kernel, we have evaluated the sensitivity of various MABL-averaged thermodynamic properties with respect to SST anomalies from a realistic high-resolution numerical simulation performed with WRF as a function of spatial scale. These sensitivities (defined with the standard coupling coefficients, that is, the slope of a linear least-squares estimator) show that the MABL–SST coupling depends strongly on the scale considered

Quarterly Journal of the Royal Meteorological Society RMetS

and different properties respond in different ways. In particular, MABL potential temperature has a monotonic coupling with SST, which increases for increasing scales. MABL humidity, instead, because of the action of VWM, displays a negative coupling peak (drier air over warmer SST) for scales smaller than 1000 km, which is mirrored by an enhanced sensitivity of LHF to the SST. We argue that this happens because the entrainment of dry air at the MABL top is proportional to the surface buoyancy flux, which increases at small scales, as controlled by the increase of SHF. This makes the enhanced entrainment-driven drying of the MABL stronger than the moistening due to the increased surface evaporation over warm SST.

To explore these processes with a minimal-physics approach, we developed a bulk model that includes MABL-averaged thermodynamic and dynamic tendencies, leveraging on the existing models by Stevens *et al.* (2002) and Neggers *et al.* (2006). With this simplified conceptual model, we have confirmed that the entrainment of dry air at the MABL top is the mechanism responsible for the observed dynamics. Firstly, by modifying the free tropospheric humidity artificially, we have shown that, if the free troposphere were more humid, the entrainment would not dry the MABL in such a way that the MABL humidity budget would be dominated by surface evaporation, which would keep the MABL close to saturation and would inhibit surface evaporation drastically. Secondly, we have used the bulk model to estimate the MABL adjustment time-scales and we have highlighted that MABL humidity reaches an equilibrium faster than MABL potential temperature. By considering a mean surface wind between 5 and 10 $\mathrm{m \cdot s^{-1}}$, the MABL adjustment time-scales of 25–45 h translate to spatial scales of about 500–1500 km, which are in the same range as the maximum coupling of LHF, wind speed, MABL height, and MABL moisture with SST.

With the scale separation method applied to the standard bulk formulae, the upscaling effect of small-scale dynamics on the large-scale LHF is also found to display a scale dependence, with a peak for scales on the order of 700–1500 km. We acknowledge that, on average, the upscaling contribution is close to zero and also its extreme values are not large and reach up to roughly 8% of the large-scale flux. However, as discussed by Busecke *et al.* (2025), who focus on western boundary currents, where such nonlinear effects are much stronger, even intermittent and localized contributions can be important for the atmospheric dynamics. In particular, in this region, such small-scale contributions can increase the spatial variability of the fluxes at scales that might trigger shallow mesoscale overturning circulations (SMOCs) in the MABL (George *et al.*, 2023). To be able to account for such possible upscaling effects, which might influence the low-level cloud mesoscale organization (Janssens *et al.*, 2023) and thus the radiative budget in this region, we suggest running new numerical simulations where the forcing SST contains different ranges of scales. This would enable us to evaluate whether some SST spatial scales resonate with MABL dynamics.

To show explicitly that the small-scale SST variability affects LHF significantly, we have also developed a LHF variance budget that relates the LHF variance to the variances of surface wind speed, SST, and surface specific humidity, and their respective covariances. This has enabled us to quantify the role of different mechanisms at different scales, indicating that, at spatial scales smaller than 1000 km, the SST spatial variability (and its covariance with the surface wind and surface humidity) dominates the LHF variance, whereas at larger scales it is the atmospheric variability that controls it.

These results are in line with Giordani *et al.* (2024), who have pointed out the increase in magnitude of turbulent kinetic energy and advective fluxes over the warm waters of the North Brazilian Current. In agreement with this, entrainment fluxes were demonstrated to take on a role in the moisture and thermal budgets of the MABL that is not negligible. These and our findings capture decisively the strong degree of thermodynamic coupling between the sea surface and atmospheric column, the primary driving force of which is the complex fine-scale structure of variability of SST and the following redistribution of buoyancy within the MABL. As the enhancement of the LHF variability is controlled by the small-scale SST variability (both directly through the Clausius–Clapeyron scaling and indirectly via the MABL adjustment), we argue that a correct representation of the low-level atmospheric mixing might feed back on the representation of surface fluxes. In the region considered here, the main ingredient for the VWM mechanism and its impact on LHF variability was the presence of a dry free atmosphere. Indeed, preliminary analyses indicate that, in the whole subtropical atmosphere, where there is large-scale subsidence, the MABL response in terms of humidity and wind speed is similar to the one observed here. This, potentially, extends the validity of the present results to a much wider area of the global ocean, increasing their relevance.

ACKNOWLEDGMENTS

This work is an outcome of the project TECLA-Dipartimenti di Eccellenza 2023–2027 funded by MUR, the Italian Ministry of University and Research. A. N. Meroni was partially supported by OGS and CINECA under HPC-TRES programme award number 2023-04. Support is acknowledged from Joint Programming Initiative Climate and Oceans (EUREC^{4}A–OA). We acknowledge the usage of AI assistants for the sole optimization of the data analysis code. Open access publishing facilitated by Universita degli Studi di Milano-Bicocca, as part of the Wiley - CRUI-CARE agreement.

CONFLICT OF INTEREST STATEMENT

The authors declare no conflicts of interest.

DATA AVAILABILITY STATEMENT

The original WRF data are available upon request to the authors of Conejero *et al.* (2024). The Python codes for the computations performed, the conceptual bulk model in use, and the data to recreate the figures in the present article may be found in the related Zenodo repository, with DOI 10.5281/zenodo.19559542. The ERA5 data used for the validation of the bulk model are accessible through the dedicated Copernicus Climate Data Store portal at: https://cds.climate.copernicus.eu/datasets.

ORCID

Alessandro Storer https://orcid.org/0009-0005-0502-871X
Matteo Borgnino https://orcid.org/0000-0002-9677-6609
Claudia Pasquero https://orcid.org/0000-0002-2211-7977
Agostino Niyonkuru Meroni https://orcid.org/0000-0001-5504-632X

REFERENCES

Acquistapace, C., Meroni, A.N., Labbri, G., Lange, D., Späth, F., Abbas, S. et al. (2022) Fast atmospheric response to a cold oceanic mesoscale patch in the north-western tropical atlantic. *Journal of Geophysical Research: Atmospheres*, 127, e2022JD036799.

Albright, A.L., Fildier, B., Touzé-Peiffer, L., Pincus, R., Vial, J. & Muller, C. (2021) Atmospheric radiative profiles during eurec 4 a. *Earth System Science Data*, 13, 617–630. Available from: https://doi.org/10.5194/essd-13-617-2021

Bian, C., Jing, Z., Wang, H., Wu, L., Chen, Z., Gan, B. et al. (2023) Oceanic mesoscale eddies as crucial drivers of global marine heatwaves. *Nature Communications*, 14, 2970. Available from: https://doi.org/10.1038/s41467-023-38811-z

Bishop, S.P., Small, R.J. & Bryan, F.O. (2020) The global sink of available potential energy by mesoscale air-sea interaction. *Journal of Advances in Modeling Earth Systems*, 12, e2020MS002118. Available from: https://doi.org/10.1029/2020MS002118

Bony, S., Stevens, B., Frierson, D.M., Jakob, C., Kageyama, M., Pincus, R. et al. (2015) Clouds, circulation and climate sensitivity. *Nature Geoscience*, 8, 261–268.

Bony, S., Schulz, H., Vial, J. & Stevens, B. (2020) Sugar, gravel, fish, and flowers: Dependence of mesoscale patterns of trade-wind clouds on environmental conditions. *Geophysical Research Letters*, 47, 1–9.

Borgnino, M., Desbiolles, F., Meroni, A. & Pasquero, C. (2025) Lower tropospheric response to local sea surface temperature anomalies: A numerical study in the eurec 4 eurec ˆ 4 a region. *Geophysical Research Letters*, 52, e2024GL112294.

Buck, A.L. (1981) New equations for computing vapor pressure and enhancement factor. *Journal of Applied Meteorology and Climatology*, 20, 1527–1532.

Busecke, J.J., Balwada, D., Martin, P.E., Nicholas, T.E., Johnson, Z.C., Nalluri, P. et al. (2025) The impact of sub-grid heterogeneity on air-sea turbulent heat flux in coupled climate models. *Geophysical Research Letters*, 52, e2025GL114951.

Chelton, D.B. & Xie, S.-P. (2010) Coupled ocean-atmosphere interaction at oceanic mesoscale. *Oceanography*, 23, 52–69.

Chelton, D.B., Schlax, M.G., Freilich, M.H. & Milliff, R.F. (2004) Satellite measurements reveal persistent small-scale features in ocean winds. *Science*, 303, 978–983.

Chen, X., Dias, J., Wolding, B., Pincus, R., Demott, C., Wick, G. et al. (2023) Ubiquitous sea surface temperature anomalies increase spatial heterogeneity of trade wind cloudiness on daily time scale. *Journal of the Atmospheric Sciences*, 80, 2969–2987.

Chin, T.M., Vazquez-Cuervo, J. & Armstrong, E.M. (2017) A multi-scale high-resolution analysis of global sea surface temperature. *Remote Sensing of Environment*, 200, 154–169.

Conejero, C., Renault, L., Desbiolles, F., McWilliams, J.C. & Giordani, H. (2024) Near-surface atmospheric response to meso- and submesoscale current and thermal feedbacks. *Journal of Physical Oceanography*, 54, 823–848. Available from: https://doi.org/10.1175/JPO-D-23-0211.1

Conejero, C., Renault, L., Desbiolles, F. & Giordani, H. (2025) Unveiling the influence of the daily oceanic (sub)mesoscale thermal 2 feedback to the atmosphere. Under Revision.

Desbiolles, F., Alberti, M., Hamouda, M.E., Meroni, A.N. & Pasquero, C. (2021) Links between sea surface temperature structures, clouds and rainfall: Study case of the mediterranean sea. *Geophysical Research Letters*, 48, e2020GL091839. Available from: https://doi.org/10.1029/2020GL091839

Dyer, A. (1974) A review of flux-profile relationships. *Boundary-Layer Meteorology*, 7, 363–372.

Fernández, P., Speich, S., Borgnino, M., Meroni, A.N., Desbiolles, F. & Pasquero, C. (2023) On the importance of the atmospheric coupling to the small-scale ocean in the modulation of latent heat flux. *Frontiers in Marine Science*, 10, 1136558. Available from: https://doi.org/10.3389/fmars.2023.1136558

Fernández, P., Speich, S., Conejero, C., Renault, L., Desbiolles, F., Pasquero, C. et al. (2025) On the mechanisms driving latent heat flux variations in the northwest tropical atlantic: a modeling approach. EGUsphere [preprint].

Frenger, I., Gruber, N., Knutti, R. & Münnich, M. (2013) Imprint of southern ocean eddies on winds, clouds and rainfall. *Nature Geoscience*, 6, 608–612.

Gentemann, C.L., Clayson, C.A., Brown, S., Lee, T., Parfitt, R., Farrar, J.T. et al. (2020) Fluxsat: measuring the ocean–atmosphere turbulent exchange of heat and moisture from space. *Remote Sensing*, 12, 1796.

George, G., Stevens, B., Bony, S., Vogel, R. & Naumann, A.K. (2023) Widespread shallow mesoscale circulations observed in the trades. *Nature Geoscience*, 16, 584–589.

Giordani, H., Conejero, C. & Renault, L. (2024) Adjustment of the marine atmospheric boundary-layer to the north brazil current during the eurec4a-oa experiment. *Dynamics of Atmospheres and Oceans*, 108, 101500.

Hayes, S., McPhaden, M. & Wallace, J. (1989) The influence of sea-surface temperature on surface wind in the eastern equatorial pacific: Weekly to monthly variability. *Journal of Climate*, 2, 1500–1506.

Hersbach, H., Bell, B., Berrisford, P., Hirahara, S., Horányi, A., Muñoz-Sabater, J. et al. (2020) The era5 global reanalysis. *Quarterly Journal of the Royal Meteorological Society*, 146, 1999–2049.

Hirata, H., Kawamura, R., Yoshioka, M.K., Nonaka, M. & Tsuboki, K. (2019) Key role of the kuroshio current in the formation of frontal structure of an extratropical cyclone associated with heavy precipitation. *Journal of Geophysical Research: Atmospheres*, 124, 6143–6156.

Hong, S.-Y., Dudhia, J. & Chen, S.-H. (2004) A revised approach to ice microphysical processes for the bulk parameterization of clouds and precipitation. *Monthly Weather Review*, 132, 103–120. Available from: https://doi.org/10.1175/1520-0493(2004)132

Janssens, M., De Arellano, J.V.-g., Van Heerwaarden, C.C., De Roode, S.R., Siebesma, A.P. & Glassmeier, F. (2023) Nonprecipitating shallow cumulus convection is intrinsically unstable to length scale growth. *Journal of the Atmospheric Sciences*, 80, 849–870.

Jiménez, P.A., Dudhia, J., González-Rouco, J.F., Navarro, J., Montávez, J.P. & García-Bustamante, E. (2012) A revised scheme for the wrf surface layer formulation. *Monthly Weather Review*, 140, 898–918.

Li, D. (2019) Turbulent prandtl number in the atmospheric boundary layer-where are we now? *Atmospheric Research*, 216, 86–105.

Li, Y. & Carbone, R.E. (2012) Excitation of rainfall over the tropical western pacific. *Journal of the Atmospheric Sciences*, 69, 2983–2994. Available from: https://doi.org/10.1175/JAS-D-11-0245.1

McWilliams, J.C. (2016) Submesoscale currents in the ocean. *Proceedings of the Royal Society A: Mathematical, Physical and Engineering Sciences*, 472, 20160117.

Medeiros, B. & Nuijens, L. (2016) Clouds at barbados are representative of clouds across the trade wind regions in observations and climate models. *Proceedings of the National Academy of Sciences of the United States of America*, 113, E3062–E3070.

Minobe, S., Kuwano-Yoshida, A., Komori, N., Xie, S.-P. & Small, R.J. (2008) Influence of the gulf stream on the troposphere. *Nature*, 452, 206–209 http://www.ncbi.nlm.nih.gov/pubmed/18337820

Naumann, A.K., Stevens, B. & Hohenegger, C. (2019) A moist conceptual model for the boundary layer structure and radiatively driven shallow circulations in the trades. *Journal of the Atmospheric Sciences*, 76, 1289–1306.

Neggers, R., Stevens, B. & Neelin, J.D. (2006) A simple equilibrium model for shallow-cumulus-topped mixed layers. *Theoretical and Computational Fluid Dynamics*, 20, 305–322.

Njouodo, N.A.S., Koseki, S., Keenlyside, N. & Rouault, M. (2018) Atmospheric signature of the agulhas current. *Geophysical Research Letters*, 45, 5185–5193.

Parfitt, R., Czaja, A., Minobe, S. & Kuwano-Yoshida, A. (2016) The atmospheric frontal response to sst perturbations in the gulf stream region. *Geophysical Research Letters*, 43, 2299–2306.

Renault, L., Contreras, M., Marchesiello, P., Conejero, C., Uchoa, I. & Wenegrat, J. (2024) Unraveling the impacts of submesoscale thermal and current feedbacks on the low-level winds and oceanic submesoscale currents. *Journal of Physical Oceanography*, 54, 2463–2486.

Romps, D.M. (2017) Exact expression for the lifting condensation level. *Journal of the Atmospheric Sciences*, 74, 3891–3900.

Seo, H., O'Neill, L.W., Bourassa, M.A., Czaja, A., Drushka, K., Edson, J.B. et al. (2023) Ocean mesoscale and frontal-scale ocean–atmosphere interactions and influence on large-scale climate: A review. *Journal of Climate*, 36, 1981–2013.

Sherwood, S.C., Bony, S. & Dufresne, J.L. (2014) Spread in model climate sensitivity traced to atmospheric convective mixing. *Nature*, 505, 37–42.

Skamarock, W.C., Klemp, J.B., Dudhia, J., Gill, D.O., Liu, Z., Berner, J. et al. (2019) *A Description of the Advanced Research WRF Model Version 4*, Vol. 145. Boulder, CO, USA: National Center for Atmospheric Research, 550

Small, R.J., de Szoeke, S.P., Xie, S.-P., O'Neill, L.W., Seo, H., Song, Q. et al. (2008) Air-sea interaction over ocean fronts and eddies. *Dynamics of Atmospheres and Oceans*, 45, 274–319.

Stevens, B. (2006) Bulk boundary-layer concepts for simplified models of tropical dynamics. *Theoretical and Computational Fluid Dynamics*, 20, 279–304.

Stevens, B., Duan, J., McWilliams, J.C., Münnich, M. & Neelin, J.D. (2002) Entrainment, rayleigh friction, and boundary layer winds over the tropical pacific. *Journal of Climate*, 15, 30–44.

Stevens, B., Bony, S., Farrell, D., Ament, F., Blyth, A., Fairall, C. et al. (2021) EUREC^{4}A. *Earth System Science Data*, 13, 4067–4119.

Storer, B.A., Buzzicotti, M., Khatri, H., Griffies, S.M. & Aluie, H. (2022) Global energy spectrum of the general oceanic circulation. *Nature Communications*, 13, 5314. Available from: https://doi.org/10.1038/s41467-022-33031-3

Storer, A., Borgnino, M., Meroni, A.N., Desbiolles, F., Conejero, C., Renault, L. et al. (2025) Response of the atmospheric boundary layer to sst variability in a coupled simulation in the atlantic trades. *Advances in Science and Research*, 22, 103–110. Available from: https://doi.org/10.5194/asr-22-103-2025

Stull, R.B. (2012) *An Introduction to Boundary Layer Meteorology*, Vol. 13. Dordrecht, Netherlands: Springer Science & Business Media.

Tartaglione, N., Desbiolles, F., del Moral-Méndez, A., Meroni, A.N., Napoli, A., Borgnino, M. et al. (2024) Low cloud response to aerosol-radiation-cloud interactions: Idealized wrf numerical experiments for eurec4a project. *Atmospheric Science Letters*, 25, e1208.

Vogel, R., Bony, S. & Stevens, B. (2020) Estimating the shallow convective mass flux from the subcloud-layer mass budget. *Journal of the Atmospheric Sciences*, 77, 1559–1574.

Wallace, J., Mitchell, T. & Deser, C. (1989) The influence of sea surface temperature on surface wind in the eastern equatorial pacific: Seasonal and interannual variability. *Journal of Climate*, 2, 1492–1499.

Zelinka, M.D., Myers, T.A., McCoy, D.T., Po-Chedley, S., Caldwell, P.M., Ceppi, P. et al. (2020) Causes of higher climate sensitivity in cmip6 models. *Geophysical Research Letters*, 47, e2019GL085782.

Zheng, Y. (2019) Theoretical understanding of the linear relationship between convective updrafts and cloud-base height for shallow cumulus clouds. part i: Maritime conditions. *Journal of the Atmospheric Sciences*, 76, 2539–2558.

How to cite this article: Storer, A., Borgnino, M., Pasquero, C. & Meroni, A.N. (2026) Scale dependence of the marine atmospheric boundary-layer response to ocean surface-temperature variability in the EUREC^{4}A region. *Quarterly Journal of the Royal Meteorological Society*, e70244. Available from: https://doi.org/10.1002/qj.70244

APPENDIX A. BULK MODEL EQUATIONS AND VALIDATION

The model is composed of the following equations:

$$\frac{dh}{dt} = E - Dh - M, \tag{A1}$$
$$\frac{d\theta_l}{dt} = \frac{1}{h}S_{\theta_l} + E_{\theta_l} + F_{\mathrm{adv},\theta_l} + F_{\mathrm{rad}}, \tag{A2}$$
$$\frac{dq_t}{dt} = \frac{1}{h}S_{q_t} + E_{q_t} + F_{\mathrm{adv},q_t}, \tag{A3}$$
$$\frac{dU}{dt} = f(V - V^+) + \frac{1}{h}S_U + E_U + F_{\mathrm{adv},U}, \tag{A4}$$
$$\frac{dV}{dt} = -f(U - U^+) + \frac{1}{h}S_V + E_V + F_{\mathrm{adv},V}, \tag{A5}$$

where

- the E terms represent the entrainment at the MABL top and, physically, involve the vertical turbulent mixing of the free tropospheric properties in the MABL;
- D is the vertically integrated boundary layer large-scale divergence (kept constant) and is typically positive in regions of large-scale subsidence;
- M is the convective mass flux related to shallow convection, which characterizes the low-level cumuli observed in the region;
- S terms are surface turbulent exchanges and account for sensible and latent heat flux for temperature and humidity, respectively, as well as surface drag for the horizontal momentum components;
- F terms include advection of all properties due to the large-scale atmospheric circulation and the radiative cooling term;
- f is the Coriolis parameter that appears in the Coriolis acceleration for the horizontal wind.

Surface exchanges are computed with the standard bulk formulations:

$$S_{\theta_l} = C_{\theta_l}|\boldsymbol{U}_s|(\theta_{ls} - \theta_l), \tag{A6}$$
$$S_{q_t} = C_{q_t}|\boldsymbol{U}_s|(q_s^* - q_t), \tag{A7}$$
$$S_U = -C_D|\boldsymbol{U}_s|U, \tag{A8}$$
$$S_V = -C_D|\boldsymbol{U}_s|V, \tag{A9}$$

with the subscript $_s$ denoting surface variables, superscript * indicating saturation, and the coefficients C indicating the surface exchange coefficients, the values of which are listed in Table A1. Surface turbulent fluxes are related to the S terms as $\mathrm{SHF} = \rho_a c_p S_{\theta_l}$ and $\mathrm{LHF} = \rho_a L_v S_{q_t}$.

The discontinuities of the atmospheric properties at the MABL top across the cloud layer are denoted with Δ and they are represented as

TABLE A1 Model constants taken from Neggers *et al.* (2006).

Variable	Description	Value [units]
Δz	Transition-layer thickness	100.0 [m]
C_{qs}	Surface moisture exchange coefficient	0.0012
$C_{\theta s}$	Surface θ_l exchange coefficient	0.0012
C^c_{qt}	Cloud-level moisture exchange coefficient	0.1
$C^c_{\theta_l}$	Cloud-level θ_l exchange coefficient	0.03
C_D	Surface wind drag coefficient	0.001
C^c_U	Cloud-level U-momentum exchange coefficient	1
C^c_V	Cloud-level V-momentum exchange coefficient	1

$$\Delta\theta_l = C^c_{\theta_l}(\theta_l^+ - \theta_l), \tag{A10}$$
$$\Delta q_t = C^c_{q_t}(q_t^+ - q_t), \tag{A11}$$
$$\Delta U = C^c_U(U^+ - U), \tag{A12}$$
$$\Delta U = C^c_V(V^+ - V), \tag{A13}$$

with the coefficients C^c representing the effects of the cloud layer, also indicated in Table A1.

The entrainment at the top of the boundary layer is directly proportional to the surface virtual potential temperature flux $S_{\theta_v} = (1 + 0.61q_s^*)S_{\theta_l} + 0.61\theta_{ls}S_{q_t}$ and inversely proportional to the virtual potential temperature jump at the MABL top $\Delta\theta_v = \Delta\theta_l + 0.61(q_t\Delta\theta_l + \theta_l\Delta q_t + \Delta\theta_l\Delta q_t)$, namely

$$E = 0.2\frac{S_{\theta_v}}{\Delta\theta_v}. \tag{A14}$$

This term controls all other entrainment terms as

$$E_{\theta_l} = \frac{1}{h}E\Delta\theta_l, \tag{A15}$$
$$E_{q_t} = \frac{1}{h}E\Delta q_t, \tag{A16}$$
$$E_U = \frac{Pr}{h}E\Delta U, \tag{A17}$$
$$E_V = \frac{Pr}{h}E\Delta V, \tag{A18}$$

where Pr indicates the turbulent Prandtl number and convert the entrainment rate of temperature and humidity into the horizontal momentum entrainment rate. We employ the formulation of Pr by Dyer (1974) (and recently reviewed by Li, 2019), which defines it as a function of the ratio between the reference height (which we set equal

Quarterly Journal of the Royal Meteorological Society RMetS

to 10 m) and Monin–Obukhov length. We considered 90% of the bulk wind speed in the computation of the friction velocity: this fraction represents the ratio between the wind speed at 10 m and the depth-integrated profile within the MABL, as retrieved from the high-resolution simulation dataset, described in the next section.

The convective mass flux M is represented as the product between a convective vertical velocity scale w^* and an area fraction a_c. The velocity scale is the Deardorff velocity (Stull, 2012):

$$w^* = \left(h\, g \frac{S_{\theta_v}}{\theta_v} \right)^{1/3}, \tag{A19}$$

with g indicating the gravitational acceleration and $\theta_v = \theta_l(1 + 0.61 q_t)$ the MABL virtual potential temperature. The area fraction depends on the normalized sub-saturation at the MABL top as

$$a_c = \frac{1}{2} + 0.36 \arctan\left(1.55 \frac{q_t - q_h^*}{\sigma_q} \right), \tag{A20}$$

with q_h^* being the saturation specific humidity at the MABL top computed from the saturation water-vapour pressure after Buck (1981), then converted to specific humidity assuming a surface pressure of 1015 hPa and following the hydrostatic pressure profile up to the MABL top. σ_q, instead, is the humidity variance and is expressed as

$$\sigma_q = \left(-\frac{S_{q_t}}{w^*} \frac{\Delta q_t}{\Delta z} h \right)^{1/2}, \tag{A21}$$

with Δz being the depth of the transition layer above the MABL (kept constant).

The mixed layer is designed to be constantly cloud-free and the convective area fraction is meant to account for the development of convective clouds breaking the transition-layer inversion. To the authors' knowledge, the literature does not provide any means for a straightforward translation of a_c to the more common cloud-fraction metric, even if links between the two quantities have been pointed out (Stevens, 2006).

Table A1 specifies all constant parameters that are used in the model. The remaining terms of the equations involving advection and radiative cooling are fixed boundary conditions and are defined in Table 1 in the main text.

Following the approach of Neggers *et al.* (2006), we assess how the output of the simple bulk model compares with the ERA5 (Hersbach *et al.*, 2020) climatological statistics for February (1990–2020 average). We limited the region of interest for this validation to the northwestern tropical and subtropical Atlantic. As boundary conditions, we selected thermodynamic variables at 800 hPa (representative of the top edge of the cloud layer and the trade-wind inversion) and wind speed at 950 hPa, representing values just above the mixed layer. Thermodynamic advective tendencies were estimated from the wind, humidity, and potential temperature fields averaged over the four levels closest to surface (1000–900 hPa): representative values that we obtained for the domain under consideration are $F_{\mathrm{adv},q} = -1\ \mathrm{g \cdot kg^{-1} \cdot day^{-1}}$ and $F_{\mathrm{adv},\theta} = -1\ \mathrm{K \cdot day^{-1}}$. Radiative cooling was kept to the reconstructed clear-sky, boundary-layer average value of $F_{\mathrm{rad}} = -2\ \mathrm{K \cdot day^{-1}}$ following the EUREC^{4}A campaign data (Albright *et al.*, 2021).

The first column of Figure A1 displays the resulting mixed-layer height h, specific humidity q_t, liquid water potential temperature θ_l, wind speed U, latent and (LHF), and sensible (SHF) heat fluxes, compared with the same quantities obtained from the ERA5 reanalysis (second column). Overall, except for the MABL height h, all atmospheric variables have similar spatial structures, indicating that the bulk model reproduces the climatological atmospheric state reasonably well. Fractional differences between the respective fields (third column) allow us to state more practically that the bulk model captures remarkably well the distribution and values of the low-level ERA5 potential temperature, generally underestimating it by 1%, and of wind speed, for which the underestimation is smaller than 15%. It tends, nonetheless, to overestimate the low-level specific humidity by 15%–30% and computes a mixed-layer height that is generally shallower than ERA5 boundary-layer height. In particular, mixed-layer height values decrease in the northward direction. This seems to be related to the underestimation of LHF in the same northward part of the domain considered, possibly because of a combined effect of the underestimation of the wind speed and overestimation of MABL humidity. Sensible heat fluxes appear to be underestimated by about 30%–40%, even if there appears to be a better degree of correlation between the bulk and ERA5 fields.

Despite these discrepancies, we believe that the bulk model captures the physical processes to be used for the purposes of this work reasonably well.

A.1 Scale separation of the surface turbulent fluxes

We provide here (Figure A2) some snapshots of SST′ and LHF′ for different kernel width, according to the scale selection carried out with the Gaussian filter: once should appreciate that, at smaller scales, the two anomaly fields are highly spatially correlated.

To link environmental variables consistently with the surface turbulent fluxes, we display here the full linearization of the bulk SHF and LHF, with the definition of the γ and λ functions correspondingly. By separating the spatial scales for the terms that appear in the SHF, one can write

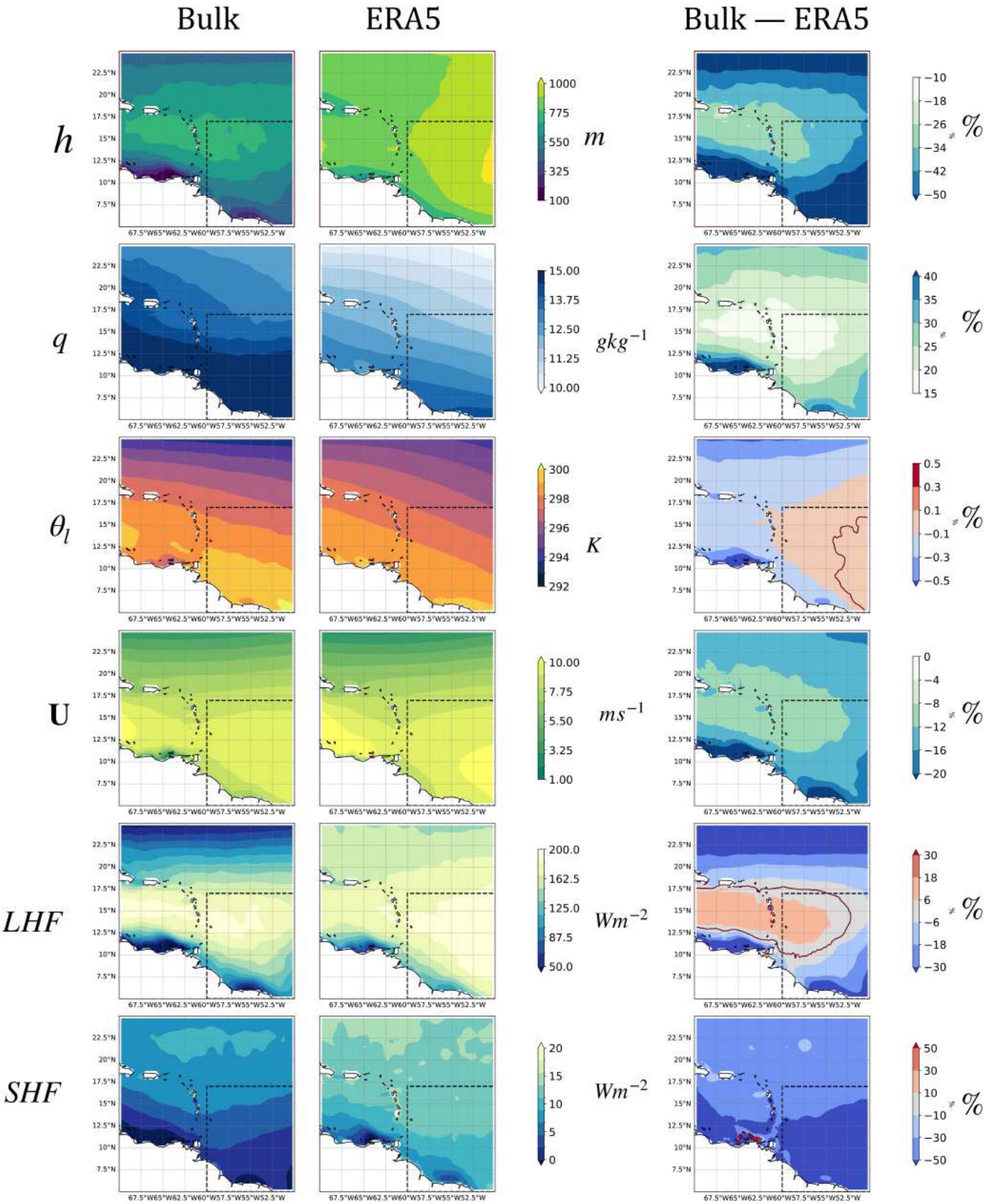

FIGURE A1 Left column: equilibrium variables from the model integration, with ERA5 boundary forcing fields. Centre column: ERA5 state variables. Right column: fractional differences between the prognostic variables from the bulk model integration and ERA5. [Colour figure can be viewed at wileyonlinelibrary.com]

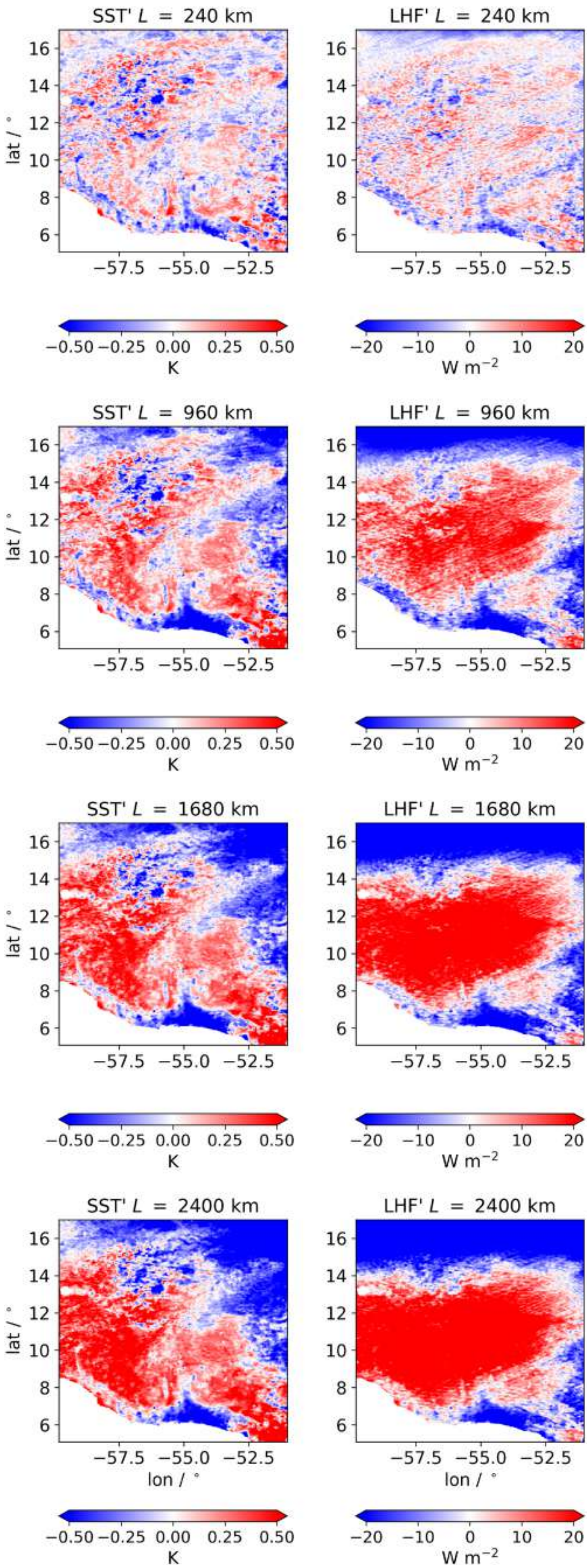

FIGURE A2 High-pass filtered SST and LHF with varying filter length-scale L. [Colour figure can be viewed at wileyonlinelibrary.com]

$$
\begin{aligned}
\mathrm{SHF} &= \beta_{\mathrm{h}}(\overline{\langle U\rangle} + \langle U\rangle')\left[\overline{\mathrm{SST}} + \mathrm{SST}' - \overline{\langle\theta_{\mathrm{l}}\rangle} - \langle\theta_{\mathrm{l}}\rangle'\right] \\
&= \beta_{\mathrm{h}}\overline{\langle U\rangle}\left[\overline{\mathrm{SST}} - \overline{\langle\theta_{\mathrm{l}}\rangle}\right] + \beta_{\mathrm{h}}\left[\overline{\mathrm{SST}} - \overline{\langle\theta_{\mathrm{l}}\rangle}\right]\langle U\rangle' \\
&\quad + \beta_{\mathrm{h}}\overline{\langle U\rangle}\mathrm{SST}' - \beta_{\mathrm{h}}\overline{\langle U\rangle}\langle\theta_{\mathrm{l}}\rangle' + O'',
\end{aligned}
\tag{A22}
$$

from which the definition of the γ functions naturally arises, namely

$$\gamma_{\langle U\rangle} = \beta_{\mathrm{h}}(\overline{\mathrm{SST}} - \overline{\langle\theta_{\mathrm{l}}\rangle}), \tag{A23}$$

$$\gamma_{\mathrm{SST}} = \beta_{\mathrm{h}}\overline{\langle U\rangle}, \tag{A24}$$

$$\gamma_{\langle\theta_{\mathrm{l}}\rangle} = -\beta_{\mathrm{h}}\overline{\langle U\rangle}. \tag{A25}$$

Similarly, for LHF, by making use of a first-order Taylor expansion in the scale-separation of the saturation specific humidity $q^*(\mathrm{SST})$, one can write

$$
\begin{aligned}
\mathrm{LHF} &= \beta_{\mathrm{e}}(\overline{\langle U\rangle} + \langle U\rangle')\left[q^*(\overline{\mathrm{SST}} + \mathrm{SST}') - \overline{\langle q\rangle} - \langle q\rangle'\right] \\
&= \beta_{\mathrm{e}}(\overline{\langle U\rangle} + \langle U\rangle') \\
&\quad \left[q^*(\overline{\mathrm{SST}}) + \left.\frac{\partial q^*}{\partial \mathrm{SST}}\right|_{\overline{\mathrm{SST}}}\mathrm{SST}' - \overline{\langle q\rangle} - \langle q\rangle'\right] \\
&= \beta_{\mathrm{e}}\overline{\langle U\rangle}\left[q^*(\overline{\mathrm{SST}}) - \overline{\langle q\rangle}\right] + \beta_{\mathrm{e}}\left[q^*(\overline{\mathrm{SST}})\right. \\
&\quad \left. - \overline{\langle q\rangle}\right]\langle U\rangle' + \beta_{\mathrm{e}}\overline{\langle U\rangle}\left.\frac{\partial q^*}{\partial \mathrm{SST}}\right|_{\overline{\mathrm{SST}}}\mathrm{SST}' \\
&\quad - \beta_{\mathrm{e}}\overline{\langle U\rangle}\langle q\rangle' + O'',
\end{aligned}
\tag{A26}
$$

from which the definition of the λ functions follows as

$$\lambda_{\langle U\rangle} = \beta_{\mathrm{e}}\left[q^*(\overline{\mathrm{SST}}) - \overline{\langle q\rangle}\right], \tag{A27}$$

$$\lambda_{\mathrm{SST}} = \beta_{\mathrm{e}}\overline{\langle U\rangle}\cdot\left.\frac{\partial q^*}{\partial \mathrm{SST}}\right|_{\overline{\mathrm{SST}}}, \tag{A28}$$

$$\lambda_q = -\beta_{\mathrm{e}}\overline{\langle U\rangle}. \tag{A29}$$

A.2 Bulk-model equilibrium solution dependence on the SST

This motivates the use of the bulk model equations (Equations A1–A5) to evaluate the dominant terms that explain the dependence of the solution on variation of SST. To do so, we compute all terms of the tendency equations at equilibrium for a range of SST values that correspond to the space and time variability of the SST used in the WRF simulation. In particular, we consider the range comprised the 5th–95th percentiles of the SST distribution, namely between 298 and 301 K.

It appears that, among the h tendency terms, entrainment increases with SST and is always slightly larger in absolute value than the mass flux, as their difference is equal to the small negative term related to the large-scale subsidence. The slightly faster increase of E with SST

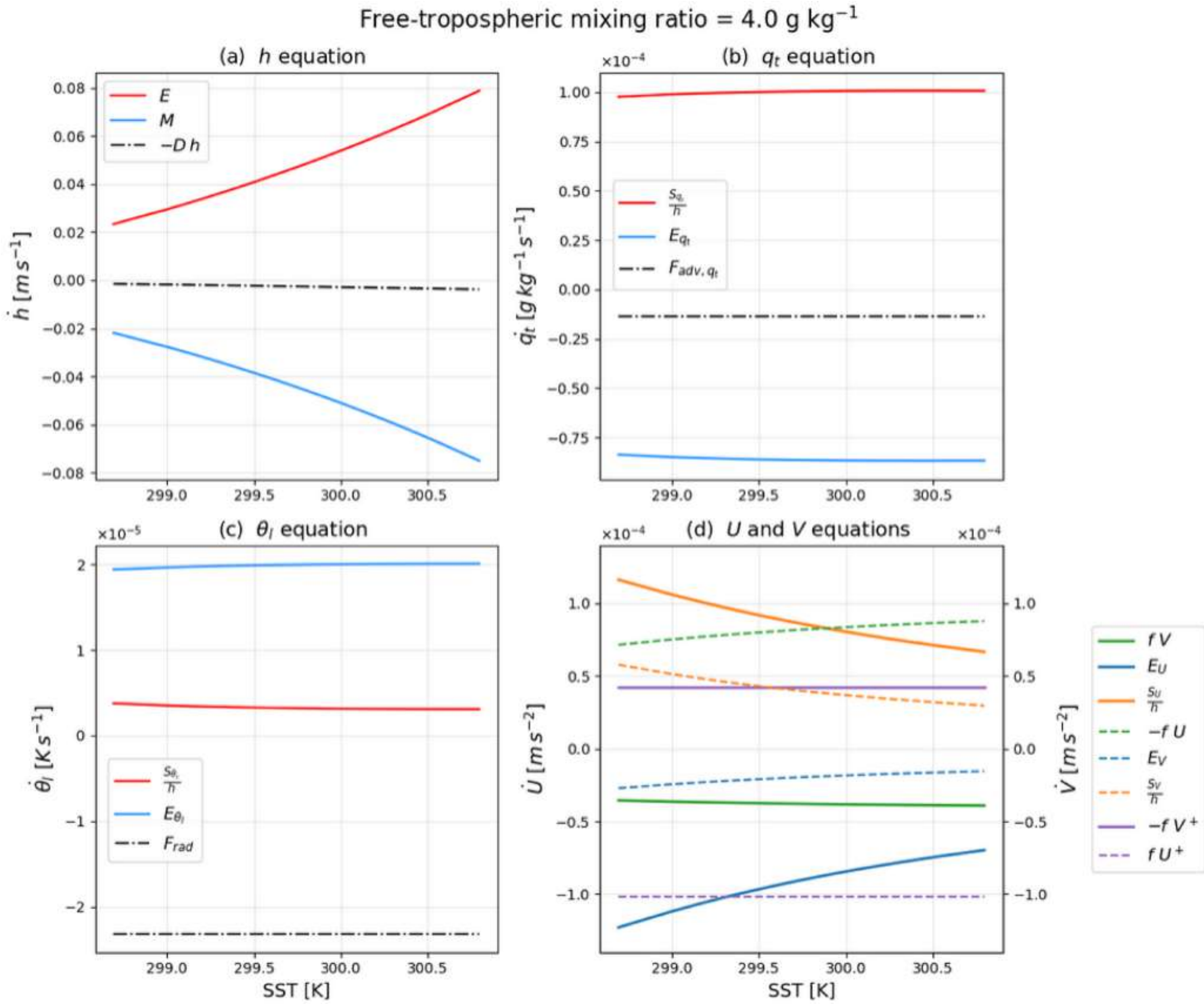

FIGURE A3 Sensitivities of all the single forcing terms in Equations (A1–A5) at equilibrium. [Colour figure can be viewed at wileyonlinelibrary.com]

explains the growth in h (Figure A3a). Concerning θ_l, balance is accomplished mainly via entrainment-driven warming at the MABL top and cooling due to longwave radiation emission (Figure A3c), whereas for q_t the dominant terms are surface evaporation and drying due to the MABL-top entrainment (Figure A3b), with little dependence on SST. As stated in Equations (A3) and (A2), the surface fluxes and entrainment enter the tendency equations for θ_l and q_t normalized by the boundary-layer depth h, hence their increase with SST is hidden by the growth of the denominator in the equations. The balance for horizontal momentum components is mainly between surface drag and entrainment for the zonal direction (full orange and blue lines in Figure A3d); that for the meridional component is between drag and the sum of the pressure and Coriolis terms (dashed orange, purple, and green lines). This asymmetry is reasonable in light of the predominantly zonal direction of the flow at tropical latitudes (Stevens *et al.*, 2002).

A.3 Dessication is more important than mixed-layer growth in the bulk model

We started from the equilibrium condition for q_t, therefore imposing $\partial q_t/\partial t = 0$, and by making terms in Equation (A3) explicit:

$$C_q U\,(q^* - q_t) = -C_h E\,(q^+ - q_t) - h \cdot F_{adv,q}. \qquad (A30)$$

One may then isolate the equilibrium value of q_t to get

$$q_t = C_q\,\frac{Uq^*}{C_h E + C_q U} + C_H q^+ \frac{E}{C_h E + C_q U} + F_a \frac{h}{C_h E + C_q U} \qquad (A31)$$

and, by applying the derivative with respect to the SST to both sides, obtain

$$\frac{\partial q_{\mathrm{t}}}{\partial SST} = \frac{1}{(C_q U + C_H E)^2} \cdot \left[\frac{\partial U}{\partial SST} \left(C_q C_H E q^* - C_q C_H q^+ E - C_q F_{\mathrm{a}} h \right) + \frac{\partial E}{\partial SST} \left(-C_q C_H U q^* + C_q C_H U q^+ - C_H F_{\mathrm{a}} h \right) + \frac{\partial q^*}{\partial SST} \left(C_q C_H E U + C_q^2 U^2 \right) + \frac{\partial h}{\partial SST} \left(C_H E F_{\mathrm{a}} + C_q U F_{\mathrm{a}} \right) \right]. \quad \text{(A32)}$$

By computing these terms with the values from the bulk model integrations, the entrainment sensitivity to SST appears to be the largest in magnitude and the one forcing a net reduction (negative sign) in the equilibrium moisture mixing ratio, forcing a $-2\ g \cdot kg^{-1} \cdot K^{-1}$ decrease; the change in h with SST also decreases the mixed-layer water vapour concentration, with magnitude about $-0.25\ g \cdot kg^{-1} \cdot K^{-1}$ (Figure A4).

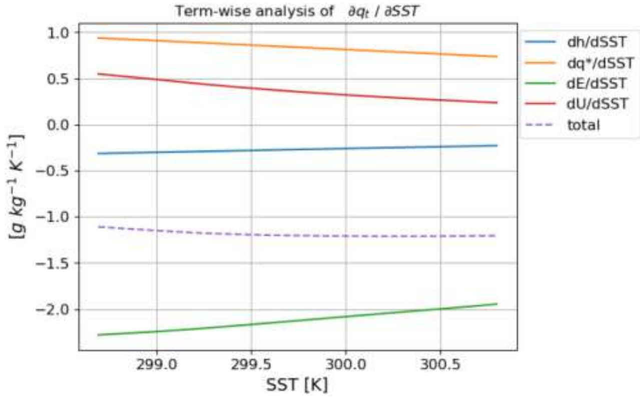

FIGURE A4 Dependence of the equilibrium MABL humidity as a function of the forcing SST. The entries in the legend only show the derivative term of the decomposition of Equation (A35). [Colour figure can be viewed at wileyonlinelibrary.com]